Remodelling the evolution of grain size distribution in galaxies

Hiroyuki Hirashita[*] and Shohei Aoyama

Institute of Astronomy and Astrophysics, Academia Sinica, Astronomy-Mathematics Building, AS/NTU No. 1, Sec. 4, Roosevelt Road, Taipei 10617, Taiwan

ABSTRACT

We revisit the evolution model of grain size distribution in a galaxy for the ultimate purpose of implementing it in hydrodynamical simulations. We simplify the previous model in such a way that some model-dependent assumptions are replaced with simpler functional forms. For the first test of the developed framework, we apply it to a one-zone chemical evolution model of a galaxy, confirming that our new model satisfactorily reproduces the previous results and that efficient coagulation of small grains produced by shattering and accretion is essential in reproducing the so-called MRN grain size distribution. For the next step, in order to test if our model can be treated together with the hydrodynamical evolution of the interstellar medium (ISM), we post-process a hydrodynamical simulation of an isolated disc galaxy using the new grain evolution model. We sample hydrodynamical particles representing each of the dense and diffuse ISM phases. By this post-processing, we find that the processes occurring in the dense gas (grain growth by accretion and coagulation) are important in reproducing the grain size distribution consistent with the Milky Way extinction curve. In our model, the grain size distributions are similar between the dense and diffuse ISM, although we observe a larger dispersion in the dense ISM. Moreover, we also show that even if we degrade the grain radius resolution (with 16 grid points), the overall shape of grain size distribution (and of resulting extinction curve) can be captured.

Key words: methods: numerical – dust, extinction – galaxies: evolution – galaxies: ISM – galaxies: spiral.

1 INTRODUCTION

The evolution of dust in the interstellar medium (ISM) plays a fundamental role in characterizing the galaxy evolution. Dust modifies the appearance of galaxies by absorbing and scattering the stellar light and reemitting it into the far-infrared (FIR).[1] Thus, dust shapes the observed spectral energy distributions (SEDs) of galaxies from ultraviolet (UV) to FIR (e.g. Takeuchi et al. 2005). Dust surfaces are the main site for the formation of some molecular species, especially H_2 (e.g. Gould & Salpeter 1963; Cazaux & Tielens 2004), giving rise to molecular-rich environments or molecular clouds, which host star formation (e.g. Hirashita & Ferrara 2002; Chen et al. 2018). Dust also affects the thermal evolution of star-forming clouds by radiating away the thermal energy (i.e. dust cooling). In the later stage of star formation, dust cooling induces fragmentation (Omukai et al. 2005) and determines the typical stellar mass (Schneider et al. 2006).

The above important processes are not only scaled with the total dust abundance but also affected by the grain size distribution. In particular, the grain size distribution is important in determining the efficiencies of grain surface reaction rates (Yamasawa et al. 2011; Harada et al. 2017) and the wavelength dependence of dust opacity (e.g. Mathis, Rumpl & Nordsieck 1977, hereafter MRN). Therefore, we have to understand the evolutions of both total dust abundance and grain size distribution. The total dust abundance is predominantly determined by stellar dust production, dust growth (accretion of gas-phase materials), and dust destruction [sputtering in supernova (SN) shocks] (e.g. Dwek 1998; Zhukovska, Gail & Trieloff 2008), while the grain size distribution is determined by shattering (grain fragmentation) and coagulation (grain–grain sticking) in addition to the above processes (e.g. Asano et al. 2013, hereafter A13). In fact, as pointed out by Kuo & Hirashita (2012), the total dust abundance is also affected by the grain size distribution because grain growth by accretion occurs in a way dependent on the total grain surface area. This indicates that the dust evolution model should include the two aspects (total dust abundance and grain size distribution) in a consistent manner.

Recently, there have been some efforts of consistently modelling the evolution of total dust abundance and grain size distribution. A13 constructed a full framework for treating the evolution of grain size distribution throughout the entire galactic evolution. After such an effort, the evolution of grain size distribution is found to be

[1] In this paper, we use the term FIR for the wavelength range where the emission is dominated by dust.

roughly described in the following way. At the early metal-poor stage of galactic evolution, the dust is predominantly supplied from SNe (Kozasa, Hasegawa & Nomoto 1989; Todini & Ferrara 2001; Nozawa et al. 2003; Bianchi & Schneider 2007; Cherchneff & Dwek 2010) and asymptotic giant branch (AGB) stars (e.g. Ferrarotti & Gail 2006; Valiante et al. 2009; Ventura et al. 2014). In this phase, shattering gradually produces small grains (e.g. Hirashita 2012). When the system is enriched with metals, small grains produced by shattering start to accrete a significant amount of gas-phase metals in the dense ISM because small grains have large surface-to-volume ratios compared with large grains (Kuo & Hirashita 2012). As a consequence, the abundance of small grains drastically increases. This dust growth mechanism (accretion) dominates the dust mass in galaxies whose metallicity is higher than $\sim$0.1–0.3 $Z_{\odot}$ (e.g. Dwek 1998; Zhukovska et al. 2008). Afterwards, coagulation in dense clouds converts small grains to large grains. Therefore, the small grain abundance is the most enhanced relative to the total dust abundance at $\sim$0.3 $Z_{\odot}$, which means that the extinction curve is the steepest at sub-solar metallicity (Hou et al. 2017).

Dust evolution models have recently been included in hydrodynamical simulations of galaxies for the purpose of obtaining a consistent understanding between the dust and ISM evolution. Although dust could be roughly modelled by assuming a tight relation with metallicity (Yajima et al. 2014), some of the processes driving dust evolution (accretion, coagulation, shattering, and destruction) are affected by the density and temperature of the ISM as well as the metallicity. Therefore, it is desirable to model dust and the ISM consistently. Hydrodynamical simulations provide viable methods of computing the evolution of the ISM. There have been some studies incorporating dust evolution in galaxy-scale or cosmological hydrodynamical simulations. Dayal, Hirashita & Ferrara (2010) computed dust production and destruction in a cosmological simulation and predicted the FIR luminosities of high-redshift galaxies based on their models of Lyman α emitters and Lyman break galaxies. Bekki (2015) treated dust as a separate component and calculated the dust evolution under the interaction with gas, stars, and dark matter. As an application, they also incorporated H_2 formation on dust surfaces in a consistent manner with dust abundance evolution to investigate the spatial distribution of dust and molecular gas in galaxies (see also Bekki 2013). McKinnon, Torrey & Vogelsberger (2016) solved dust evolution in cosmological zoom-in simulations. They broadly reproduced the relation between dust-to-gas ratio and various quantities in galaxies, but they still needed a more realistic treatment of dust destruction and feedback by SNe. McKinnon et al. (2017) extended their model to full-volume cosmological predictions, which are useful to examine statistical properties of dust, especially, the dust mass function and the comoving dust mass density. Their simulation broadly reproduced the relevant observations in the present-day Universe. Zhukovska et al. (2016) analysed the effect of dust growth by accretion on the relation between gas density and depletion (or dust-to-metal ratio) in an isolated Milky Way-like galaxy by post-processing a hydrodynamical simulation. They examined gas-temperature-dependent sticking coefficient in accretion, in order to reproduce the relation between silicon depletion and gas density. There are also some semi-analytic models for dust evolution in a cosmological volume, focusing on high-redshift galaxies (Valiante et al. 2011; Mancini et al. 2015) or including the comparison with the local Universe (Popping, Somerville & Galametz 2017; Ginolfi et al. 2018).

None of the above simulations treated the grain size distribution. As mentioned above, the grain size distribution affects the dust evolution. Implementation of grain size distributions in a galaxy-scale

or cosmological hydrodynamical simulation has not been successful (except for the recent preliminary runs in McKinnon et al. 2018), mainly because of the high computational cost. For the purpose of treating the evolution of grain size distribution within the limitation of available computational capability, Aoyama et al. (2017, hereafter A17) and Hou et al. (2017) represented the grain sizes by two size ranges divided at around $a \sim 0.03$ µm (a is the grain radius), according to the formulation by Hirashita et al. (2015). As a consequence of this two-size approximation, they succeeded in computing the spatial variations not only in the dust abundance, but also in the grain size distribution. In particular, they predicted the spatial and temporal variation in extinction curves based on the calculated grain size distributions. The two-size approximation has been applied to a simulation of clusters of galaxies by Gjergo et al. (2018). Aoyama et al. (2018) have recently extended the simulation to a cosmological volume, predicting the statistical properties of dust abundance in galaxies and in the intergalactic medium (IGM). They confirmed the evolution of grain size distribution predicted in A13's one-zone model, but at the same time, they showed that the grain size distribution has a large variety among galaxies with similar mass and metallicity (see also Hou et al. in preparation). Such a variation cannot be naturally treated by one-zone models. Moreover, the grain size distribution in the IGM can only be predicted by cosmological simulations because the IGM dust is supplied from a large number of galaxies by stellar feedback (see also Zu et al. 2011). Since the observational estimate of dust mass in the IGM depends on the grain size distribution (Ménard & Fukugita 2012), it is desirable to clarify using cosmological simulations how the grain size distribution evolves in the IGM.

Although the above two-size approximation significantly reduces the computational cost, the prediction of extinction curves under such a treatment depends on how we reconstruct the grain size distribution from the two-size information. In other words, since the entire grain size range is represented by two sizes, the precision of the predicted extinction curves is limited. Other methods that avoid treating the full grain size distribution such as the moment formulation by Mattsson (2016) also have the same problem. More sampling of grain sizes increases the predictive power of extinction curves. For more improvement of the above theoretical predictions, thus, it is a natural step to directly treat the grain size distribution without the two-size approximation or the moment formulation in galactic or cosmological simulations. McKinnon et al. (2018) have recently developed a full grain size distribution calculation and given some test cases for isolated galaxy simulations, although realistic predictions still need to wait for their future work.

There are some possibilities of reducing the computational cost in calculations of grain size distribution. In A13's model, there are some components that depend on specific assumptions or models. For example, they adopted the results of Nozawa, Kozasa & Habe (2006) for dust destruction in SN shocks, but this procedure consumes computational time and memory because it needs to read a large table for their function $\xi(a, a')$, which describes the transition probability of the grain radius from a' to a. However, as shown by Nozawa et al. (2006), the efficiency of SN destruction depends on the ambient gas density; this dependence causes uncertainties in estimating the dust destruction rate, since each SN is hardly resolved in galaxy-scale simulations. For shattering and coagulation, A13 adopted specific calculations for grain velocities from Yan, Lazarian & Draine (2004); however, the grain velocities depend on the ambient physical conditions such as gas density, magnetic field strength, ionization degree, etc. It is extremely time-consuming to consider such an environmental dependence, and most

hydrodynamical simulations on galaxy scales do not have predictive power of all the relevant physical quantities because of limited spatial resolutions. In the treatment of shattered fragments, A13 is based on Jones, Tielens & Hollenbach (1996), whose formulation contains a few material parameters, but Hirashita & Kobayashi (2013) show that a simpler treatment by Kobayashi & Tanaka (2010), who basically describe shattering with a single parameter (critical velocity for catastrophic disruption), produces satisfactorily similar results. Simplifying some of the above assumptions will save the computational cost, but still will not change the results within the modelling uncertainties.

Given the above possible simplifications, it is worth remodelling the evolution of grain size distribution. This is the first purpose of this paper. The second aim is to test if the new model gives consistent results with the previous models such as A13. The third is to investigate a possibility of implementing the new formalism in a hydrodynamic simulation. To this goal, we post-process A17's simulation of an isolated disc galaxy to derive the evolution of grain size distribution in some selected fluid elements of the ISM. This step gives us an idea about not only the suitability for the implementation into hydrodynamical codes but also the dependence of the grain size distribution on the local physical conditions in a galaxy. We also test how the calculated grain size distribution depends on the grain radius resolution, since minimizing the number of grain size grids (bins) is useful to save the computational power.

This paper is organized as follows. In Section 2, we formulate the evolution of grain size distribution. In Section 3, we apply the formulation to a one-zone model and compare it with some previous results (mainly with A13). In Section 4, we post-process a hydrodynamical simulation of an isolated disc galaxy with our newly developed model. In Section 5, we discuss some issues and prospect for our dust evolution model. In Section 6, we give the conclusion of this paper.

2 BASIC EQUATIONS

We basically follow A13's model for the evolution of grain size distribution, but simplify it as long as we do not lose the physical essence of the relevant processes. We also remove some model-dependent ingredients from A13's model, and, if necessary, replace them with simpler formulae. This simplification could be useful for the purpose of making the dust evolution model suitable for implementation in hydrodynamical simulations. For the dust evolution processes, we consider stellar dust production, dust destruction by SN shocks in the ISM, dust growth by accretion and coagulation in the dense ISM, and dust disruption by shattering in the diffuse ISM.

Since the evolution of grain size distribution is affected by the physical condition of the ISM, we need to combine the model (or the basic equations) developed in this section with an appropriate evolution model of the ISM (or a galaxy evolution model). We adopt two types of galaxy evolution models in Section 4: one is a one-zone model and the other is a hydrodynamical model. The one-zone model applied in Section 3 has an advantage of simplicity since it neglects the spatial structure of the ISM. Thus, this model is suitable for the first test of the grain size evolution model newly developed in this section. The disadvantage of the one-zone model is that we have to assume the physical condition of the ISM. To overcome this, we use a hydrodynamical simulation to calculate the spatially resolved structure of the ISM. We use (or post-process) the hydrodynamical simulation of an isolated disc galaxy to calculate the evolution of grain size distribution. Recall that, as mentioned in Section 1, one of the major purposes of this paper is to develop a grain size distribution

model that can be implemented in hydrodynamical simulations. The application in Section 4 will give a useful step to this goal.

In this section, we describe the basic equations for the evolution of grain size distribution. The grain size distribution is expressed by the grain mass distribution $\rho_d(m, t)$, which is defined such that $\rho_d(m, t) \, dm$ (m is the grain mass and t is the time) is the mass density of dust grains whose mass is between m and $m + dm$. In this paper, we assume grains to be spherical and compact, so that $m = (4\pi/3)a^3 s$, where a is the grain radius and s is the material density of dust. If we use the grain size distribution $n(a, t)$, where $n(a, t) \, da$ is the number density of dust grains with radii between a and $a + da$, it is related to the above grain mass distribution as

$$\rho_d(m, t) \, dm = \frac{4}{3}\pi a^3 s n(a) \, da, \tag{1}$$

with $dm = 4\pi a^2 s \, da$. The total dust mass density $\rho_{d, tot}(t)$ is

$$\rho_{d,tot}(t) = \int_0^\infty \rho_d(m, t) \, dm. \tag{2}$$

The gas density is given by the number density of hydrogen nuclei, n_H, or the gas mass density, $\rho_{gas} = \mu m_H n_H$ ($\mu = 1.4$ is the gas mass per hydrogen, and m_H is the mass of hydrogen atom).

The time-evolution of $\rho_d(m, t)$ is described by

$$\frac{\partial \rho_d(m, t)}{\partial t} = \left[\frac{\partial \rho_d(m, t)}{\partial t}\right]_{star} + \left[\frac{\partial \rho_d(m, t)}{\partial t}\right]_{sput}$$
$$+ \left[\frac{\partial \rho_d(m, t)}{\partial t}\right]_{acc} + \left[\frac{\partial \rho_d(m, t)}{\partial t}\right]_{shat}$$
$$+ \left[\frac{\partial \rho_d(m, t)}{\partial t}\right]_{coag} + \rho_d(m, t)\frac{d \ln \rho_{gas}}{dt}, \tag{3}$$

where the terms with subscripts 'star', 'sput', 'acc', 'shat', and 'coag' indicate the changing rates of grain mass distribution by stellar dust production, sputtering, accretion, shattering, and coagulation, respectively (those terms are evaluated below), and the last term expresses the change of ρ_d caused by the change of the background gas density (we assume that the gas and dust are dynamically coupled) (Hirashita et al. 2015). Although the equations below are written in continuous forms, we actually solve discrete forms described in Appendix B. We adopt $N = 128$ grid points for the discrete grain size distribution in a grain radius range of 3×10^{-4}–10 μm unless otherwise stated. We set $\rho_d(m, t) = 0$ at the maximum and minimum grain radii for the boundary conditions. Since the maximum radius (10 μm) is large enough, the boundary condition at the largest grain radius does not affect the calculation. The boundary condition at the lower boundary means that we do not regard 'grains' with $a < 3 \times 10^{-4}$ μm as dust grains. The discrete time-step Δt is chosen following Appendix B4. We explain the modelling for each process in each subsection below.

2.1 Stellar dust production

A certain fraction of the metals ejected from SNe and AGB stars are condensed into dust. There are some calculations of dust condensation in SNe (e.g. Kozasa et al. 1989; Todini & Ferrara 2001; Nozawa et al. 2003) and AGB stars (e.g. Ferrarotti & Gail 2006; Ventura et al. 2014; Dell'Agli et al. 2017); however, the fraction of metals eventually injected into the ISM in the form of dust is still uncertain. For SNe, a part of condensed dust is destroyed by the reverse shock before being injected into the ISM (Bianchi & Schneider 2007; Nozawa et al. 2007). The destroyed fraction depends on the

ambient gas density (which is hardly resolved in galaxy-scale simulations) and the grain size distribution. For AGB stars, there is still a difference in the total condensed dust mass among calculations (Inoue 2011; Kuo, Hirashita & Zafar 2013). Therefore (and for the sake of simplification), we choose to adopt a constant parameter (f_{in}) that describes the condensation efficiency of metals in stellar ejecta. For the metal enrichment, we utilize a chemical enrichment model that outputs the metal mass injected into the ISM per unit time and unit volume, denoted as $\dot{\rho}_Z$. In practice, we are usually able to utilize a chemical enrichment model already implemented in the hydrodynamical simulation (e.g. A17). Therefore, we assume that $\dot{\rho}_Z$ as a function of time is already given.

Based on the above concept, we can write the change of the grain size distribution by stellar dust production as

$$\left[\frac{\partial \rho_d(m, t)}{\partial t}\right]_{star} = f_{in}\dot{\rho}_Z\, m\tilde{\varphi}(m), \tag{4}$$

where $m\tilde{\varphi}(m)$ is the mass distribution function of the dust grains produced by stars, and it is normalized so that the integration for the whole grain mass range is unity. It is often convenient to consider the grain size distribution, so that we define $\varphi(a)\,da \equiv \tilde{\varphi}(m)\,dm$. The typical size of stellar dust is of the order of $\sim 0.1\,\mu$m; thus, we adopt the following lognormal form for $\varphi(a)$:

$$\varphi(a) = \frac{C_\varphi}{a} \exp\left\{-\frac{[\ln(a/a_0)]^2}{2\sigma^2}\right\}, \tag{5}$$

where C_φ is the normalization factor, σ is the standard deviation, and a_0 is the central grain radius. We adopt $\sigma = 0.47$ and $a_0 = 0.1\,\mu$m following A13, who assigned these values based on the theoretical dust condensation calculation for AGB stars by Yasuda & Kozasa (2012). Note that A13 separately treated SNe and AGB stars and adopted the grain size distribution calculated by Nozawa et al. (2007) for SN dust. The normalization is determined by

$$\int_0^\infty \frac{4}{3}\pi a^3 \varphi(a)\,da = 1, \tag{6}$$

which is equivalent to $\int m\tilde{\varphi}(m)\,dm = 1$. We adopt $f_{in} = 0.1$ (A17).

2.2 Dust destruction by SN shocks

Since dust destruction by sputtering preserves the number of dust grains (as long as dust is not completely destroyed), we can apply the continuity equation in Appendix A, obtaining (see also Hirashita et al. 2015)

$$\left[\frac{\partial \rho_d(m, t)}{\partial t}\right]_{sput} = -\frac{\partial}{\partial m}[\dot{m}\rho_d(m, t)] + \frac{\dot{m}}{m}\rho_d(m, t), \tag{7}$$

where $\dot{m} = 4\pi a^2\dot{a}$. We estimate that

$$\dot{m} = -m/\tau_{dest}(m), \tag{8}$$

where $\tau_{dest}(m)$ is the destruction time-scale as a function of grain mass. Note that some authors adopt the decreasing time-scale of grain radius, which is related to $\tau_{dest}(m)$ as $|a/\dot{a}| = 3\tau_{dest}(m)$. We estimate $\tau_{dest}(m)$ in what follows.

For the first step to obtain $\tau_{dest}(m)$, we estimate the time-scale on which the ISM is once swept by SN shocks. This is referred to as the sweeping time-scale. The sweeping time-scale is estimated by $M_{gas}/(M_s\gamma)$, where M_{gas} is the gas mass of interest, M_s is the gas mass swept by a single SN blast, and γ is the rate of SNe sweeping the gas. Since a passage of SN shock does not destroy all the swept dust, we introduce the destruction efficiency of dust grains, $\varepsilon_{dest}(m)$, which is generally a function of m [or $\varepsilon_{dest}(a)$, which is a function

of a]. Using this efficiency, we estimate the destruction time-scale as a function of grain mass as

$$\tau_{dest}(m) = \frac{M_{gas}}{\varepsilon_{dest}(m)M_s\gamma}. \tag{9}$$

Considering the uncertainty in ε_{dest}, we adopt an empirical value estimated by McKee (1989) as ~ 0.1. Since the typical grain radius in the Galactic ISM is $\sim 0.1\,\mu$m, we adopt $\varepsilon_{dest} = 0.1$ at $a = 0.1\,\mu$m and determine its dependence on a below.

If we consider thermal sputtering, the destruction rate $\dot{a}$ is independent of a (e.g. Draine & Salpeter 1979; Tielens et al. 1994; Nozawa et al. 2006). Thus, the time-scale of destruction is proportional to a. If we take relative motion between dust and gas into account, non-thermal sputtering, which weakens the dependence of the destruction time-scale on grain radius, occurs (e.g. McKee et al. 1987). However, small grains tend to be trapped in the shocked region, which enhances the a dependence of the destruction time-scale (Nozawa et al. 2006). These processes usually occur on unresolvable spatial scales in galaxy-scale hydrodynamical simulations. Therefore, for the sake of simplicity, we assume $\dot{a}$ to be constant, or $\tau_{dest}(m) = |a/\dot{a}|/3 \propto a$. This means that $\varepsilon_{dest}(m) = \varepsilon_{dest}(a) \propto a^{-1}$. Recalling that $\epsilon_{dest}(0.1\,\mu\text{m}) = 0.1$ as assumed above, and that ε_{dest} cannot exceed 1, we adopt the following formula for the destruction efficiency:[2]

$$\epsilon_{dest}(a) = 1 - \exp\left[-0.1\left(\frac{a}{0.1\,\mu\text{m}}\right)\right]. \tag{10}$$

This functional form approximately realizes two asymptotic behaviours: $\epsilon_{dest} \sim 0.1(0.1\,\mu\text{m}/a) \propto a^{-1}$ at $a \gtrsim 0.1\,\mu$m and $\varepsilon_{dest} \sim 1$ at $a \ll 0.1\,\mu$m. We adopt $M_s = 6800\,M_\odot$ (McKee 1989; Nozawa et al. 2006). The SN rate γ is tightly coupled with the chemical enrichment; thus, we presume a situation where γ as a function of time is already given (like $\dot{\rho}_Z$ above).

2.3 Dust growth by accretion

Since dust growth by accretion can be regarded as negative destruction, it can be treated in a similar way to sputtering (Appendix A):

$$\left[\frac{\partial \rho_d(m, t)}{\partial t}\right]_{sput} = -\frac{\partial}{\partial m}[\dot{m}\rho_d(m, t)] + \frac{\dot{m}}{m}\rho_d(m, t). \tag{11}$$

For accretion, the growth rate $\dot{a}$ ($\dot{m} = 4\pi a^2\dot{a}$) is estimated as

$$\dot{m} = \xi(t)m/\tau_{acc}(m), \tag{12}$$

where $\xi(t) \equiv 1 - \rho_{d, tot}(t)/\rho_Z(t)$ [$\rho_Z(t)$ is the mass density of metals in both gas and dust phases] is the fraction of metals in the gas phase and $\tau_{acc}(m)$ is the grain growth time given by (Hirashita 2012)

$$\tau_{acc}(m) = \frac{1}{3}\tau'_{acc}(a)$$

$$\tau'_{acc}(a) = \tau'_{0,acc}\left(\frac{a}{0.1\,\mu\text{m}}\right)\left(\frac{Z}{Z_\odot}\right)^{-1}\left(\frac{n_H}{10^3\,\text{cm}^{-3}}\right)^{-1}$$

$$\times \left(\frac{T_{gas}}{10\,\text{K}}\right)^{-1/2}\left(\frac{S}{0.3}\right)^{-1}, \tag{13}$$

where $\tau'_{0,acc}$ is a constant given below, Z is the metallicity (we adopt solar metallicity $Z_\odot = 0.02$ throughout this paper for the

---

[2]Alternatively, we can adopt $\epsilon_{dest}(a) = \min[0.1(0.1\,\mu\text{m}/a), 1]$, but the smooth functional form in equation (10) is convenient to avoid discontinuous behaviour in numerical calculations.

convenience in direct comparison with previous studies), n_H is the hydrogen number density, T_{gas} is the gas temperature, and S is the sticking efficiency. Hirashita (2012) obtain $\tau_{0,\,acc} = 1.61 \times 10^8$ and 0.993×10^8 yr for silicate and graphite, respectively. In this paper, we apply the silicate value unless otherwise stated. We adopt $S = 0.3$ (Leitch-Devlin & Williams 1985; Grassi et al. 2011). We assume a situation in which ρ_Z and n_H are already given; thus, the fraction of metals in the gas phase $[\xi(t)]$ and metallicity $[Z = \rho_Z/(\mu m_H n_H)]$ can be calculated. As a consequence, the combination of equations (11)–(13) is solved in a consistent manner with the abundances of metals and dust.

2.4 Shattering

The ISM is generally turbulent. In a turbulent medium, dust grains obtain random velocities through the interaction with gas and magnetic field (Yan et al. 2004). In the diffuse ISM ($n_H \lesssim 1$ cm^{-3}), the grain velocities are so large that shattering can occur in grain–grain collisions (Hirashita & Yan 2009). We basically follow Jones et al. (1994, 1996) and Hirashita & Yan (2009) for the formulation of shattering (see also Asano et al. 2013).

The time evolution of grain size distribution by shattering is expressed as

$$\left[\frac{\partial \rho_d(m,\,t)}{\partial t}\right]_{shat} = -m\rho_d(m,\,t)\int_0^\infty \alpha(m_1,\,m)\rho_d(m_1,\,t)\,dm_1$$
$$+ \int_0^\infty \int_0^\infty \alpha(m_1,\,m_2)\rho_d(m_1,\,t)\rho_d(m_2,\,t)$$
$$\times \mu_{frag}(m;\,m_1,\,m_2)dm_1 dm_2, \qquad (14)$$

where two newly introduced functions, α and μ_{frag}, are explained below. The first term on the right-hand side indicates the loss of grains with mass m by the collisions with other grains, and α indicates the collision frequency normalized to the grain masses and grain number density). If we consider collisions between grains with masses m_1 and m_2 (radii a_1 and a_2, respectively), α is expressed as

$$\alpha(m_1,\,m_2) \equiv \frac{\sigma_{1,2}v_{1,2}}{m_1 m_2}, \qquad (15)$$

where $\sigma_{1,2}$ and $v_{1,2}$ are the collisional cross-section and the relative velocity between the two grains (we explain how to evaluate $v_{1,2}$ later). We write the collisional cross-section as

$$\sigma_{1,2} = \beta\pi(a_1 + a_2)^2, \qquad (16)$$

where β effectively regulates the cross-section relative to the geometric cross-section. We assume $\beta = 1$ for simplicity (i.e. the collision cross-section is determined by the geometric cross-section), since in shattering, the grain velocities are so large that the change of grain collisional cross-section by the Coulomb interaction is negligible. The second term of the right-hand side in equation (14) indicates the generation of grains with mass m as a result of collisions between grains with masses m_1 and m_2. Note that we count the collision between m_1 and m_2 twice to consider the fragments of m_1 and m_2 separately, and $\mu_{frag}(m;\,m_1,\,m_2)$ describes the mass distribution of fragments (including the remnant) as a result of fragmentation of a grain with mass m_1 in a collision with a grain with mass m_2. Because shattering conserves the total dust mass, the following equation should hold:

$$\int_0^\infty \mu_{frag}(m;\,m_1,\,m_2)\,dm = m_1. \qquad (17)$$

The functional form of μ_{frag} will be given later. To calculate the evolution by shattering, we also need to specify the grain velocities, which are given in what follows.

The grain velocity is determined by complicated interaction between the dust grain and the ambient magnetized gas. Asano et al. (2013) used the data calculated by Yan et al. (2004), who provide the grain velocities for some representative ISM phases. However, the physical conditions of the ISM in the course of galaxy evolution are not necessarily represented by those ISM phases. Thus, it would be convenient if we could find an analytic (or empirical) formula that correctly reflects some characteristic dependence on the ambient physical condition and the grain radius for the purpose of implementation into a hydrodynamic simulation. For this purpose, we adopt the following formula for the grain velocity as a function of grain radius (Appendix C):

$$v_{gr}(a) = 1.1\mathcal{M}^{3/2}\left(\frac{a}{0.1\,\mu m}\right)^{1/2}\left(\frac{T_{gas}}{10^4\,K}\right)^{1/4}\left(\frac{n_H}{1\,cm^{-3}}\right)^{-1/4}$$
$$\times \left(\frac{s}{3.5\,g\,cm^{-3}}\right)^{1/2}\,km\,s^{-1}, \qquad (18)$$

where $\mathcal{M}$ is the Mach number of the largest eddy velocity (which is practically used here as an adjusting parameter for the grain velocity). The functional form correctly catches the general features of the dependence on various quantities at least qualitatively in the following senses: larger grains tend to have larger velocities because they tend to be coupled with larger scale gas motion; the grain velocities are higher in a higher temperature environment because the characteristic velocity is higher; the grain velocities tend to be higher in a less dense medium because of weaker gas drag (i.e. dust grains are less trapped on small scales on which the velocity dispersion of gas is small); and heavier grains tend to have higher velocities because of their larger inertia (they are more difficult to be stopped by gas drag). Although the inclusion of magnetic field makes the dependence complicated, the above dependences on various physical quantities does not change qualitatively (Yan et al. 2004). In the diffuse ISM with $n_H \sim 0.1$–0.3 cm^{-3} and $T_{gas} \sim 6000$–8000 K, large grains ($a \sim 0.1$–1 µm) achieve a velocity of ~ 10 km s^{-1}. Thus, we adopt $\mathcal{M} = 3$ for shattering. Here, $\mathcal{M}$ effectively includes the extra grain acceleration beyond the typical thermal velocity through the interaction with magnetic field.

In considering the collision rate between two grains with $v_{gr} = v_1$ and v_2, we estimate the relative velocity $v_{1,2}$ by

$$v_{1,2} = \sqrt{v_1^2 + v_2^2 - 2v_1 v_2 \mu_{1,2}}, \qquad (19)$$

where $\mu = \cos\theta$ (θ is an angle between the two grain velocities) is randomly chosen between -1 and 1 in every calculation of α (Hirashita & Li 2013).

For the grain size distribution of the fragments, A13 followed Jones et al. (1996) (see also Hirashita & Yan 2009). Formation of fragments in their model depends on some material properties in a somewhat complicated way. Hirashita & Kobayashi (2013) argued that the most important parameter is the velocity threshold for the catastrophic fragmentation (defined as the fragmentation in which more than half of the grain is disrupted). Kobayashi & Tanaka (2010)'s formalism is simply described with only one material parameter ($Q_D^\star$ introduced later), which is related to the velocity threshold for catastrophic fragmentation. Thus, we adopt Kobayashi & Tanaka (2010)'s formulation for its simplicity, and summarize it in what follows.

First, we determine the total mass of the fragments by estimating how much fraction of the dust grain is disrupted in a collision. Now we consider a collision of two dust grains with masses m_1 and m_2. We follow Kobayashi & Tanaka (2010)'s model, which assumes that the disrupted mass (ejected mass) from m_1 is proportional to

$$\phi \equiv \frac{E_{\text{imp}}}{m_1 Q_{\text{D}}^{\star}}, \tag{20}$$

where

$$E_{\text{imp}} = \frac{1}{2} \frac{m_1 m_2}{m_1 + m_2} v_{1,2}^2, \tag{21}$$

is the impact energy between m_1 and m_2, and $Q_{\text{D}}^{\star}$ is the specific impact energy that causes the catastrophic disruption (i.e. the disrupted mass is $m_1/2$). Using ϕ, the ejected mass, m_{ej}, is estimated as

$$m_{\text{ej}} = \frac{\phi}{1 + \phi} m_1. \tag{22}$$

This satisfies the following behaviours at two extremes: $m_{\text{ej}} \sim E_{\text{imp}}/Q_{\text{D}}^{\star}$ for $\phi \ll 1$ (weak collision) and $m_{\text{ej}} \sim m_1$ for $\phi \gg 1$ (strong collision). As argued in Hirashita & Kobayashi (2013), we estimate that $Q_{\text{D}}^{\star} \simeq P_1/(2s)$, where P_1 is the critical pressure given by Jones et al. (1996) ($P_1 = 3 \times 10^{11}$ and 4×10^{10} dyn cm^{-2} for silicate and graphite, respectively; and we adopt the silicate value in this paper).

Next, we set the grain size distribution of shattered fragments. We assume a power-law size distribution with an index of α_{f}, which means that the index of mass distribution is $(-\alpha_{\text{f}} + 1)/3$. We adopt $\alpha_{\text{f}} = 3.3$ in this paper (Jones et al. 1996), but we note that the value of α_{f} is not essential in determining the resulting grain size distribution as long as $\alpha_{\text{f}} < 4$ (Hirashita & Kobayashi 2013). The maximum and minimum grain masses of the fragments, $m_{\text{f, max}}$ and $m_{\text{f, min}}$, respectively, are assumed to be (Guillet, Pineau Des Forêts & Jones 2011)

$$m_{\text{f,max}} = 0.02 m_{\text{ej}}, \tag{23}$$

$$m_{\text{f,min}} = 10^{-6} m_{\text{f,max}} \tag{24}$$

[or the maximum and minimum fragment radii, $a_{\text{f, max}} = (0.02 m_{\text{ej}}/m_1)^{1/3} a_1$ and $a_{\text{f, min}} = 0.01 a_{\text{f, max}}$, respectively]. The minimum size is assumed to be $\sim 1/100$ times the maximum size, which is roughly consistent with the treatments in Jones et al. (1996) and Hirashita & Yan (2009). In the end, we obtain the fragment mass distribution including the remnant of mass $m_1 - m_{\text{ej}}$ as

$$\mu_{\text{frag}}(m, m_1, m_2) = \frac{(4 - \alpha_{\text{f}}) m_{\text{ej}} m^{(-\alpha_{\text{f}}+1)/3}}{3 \left[m_{\text{f,max}}^{\frac{4-\alpha_{\text{f}}}{3}} - m_{\text{f,min}}^{\frac{4-\alpha_{\text{f}}}{3}} \right]}$$
$$+ (m_1 - m_{\text{ej}}) \delta(m - m_1 + m_{\text{ej}}), \tag{25}$$

where $\delta(\cdot)$ is Dirac's delta function. In reality, we use the discrete formalism for the distribution of fragments (Appendix B2). Grains which become smaller than the minimum grain size (radius a_1) are removed.

2.5 Coagulation

Coagulation occurs in the dense ISM ($n_{\text{H}} \gtrsim 100$ cm^{-3}), where grain velocities induced by turbulence are small enough to allow the grains to stick with each other in grain–grain collisions. The

evolution of grain size distribution by coagulation is written in a similar way to that by shattering as

$$\left[\frac{\partial \rho_{\text{d}}(m, t)}{\partial t} \right]_{\text{coag}} = -m \rho_{\text{d}}(m, t) \int_0^\infty \alpha(m_1, m) \rho_{\text{d}}(m_1, t) \, \mathrm{d}m_1$$
$$+ \int_0^\infty \int_0^\infty \alpha(m_1, m_2) \rho_{\text{d}}(m_1, t) \rho_{\text{d}}(m_2, t)$$
$$\times m_1 \delta(m - m_1 - m_2) \, \mathrm{d}m_1 \mathrm{d}m_2. \tag{26}$$

We note that we count the same coagulation twice by treating two coagulated grains, m_1 and m_2, separately in the second term on the right-hand side.[3] For α and σ, we use the same expressions as in equations (15) and (16), respectively. For coagulation, β in equation (16) includes the sticking coefficient (we adopt $\beta = 1$ also for coagulation). We neglect the change of grain cross-section due to the Coulomb interaction, since the kinetic energy of grains is much higher than the typical Coulomb potential energy.[4]

We adopt equation (18) for the grain velocity (with $\mathcal{M} = 1$, which roughly mimics the velocity level calculated by Yan et al. 2004 for the dense clouds) and use the same method to estimate the relative velocity as applied for shattering (equation 19). A13's model assumed a threshold velocity beyond which coagulation is prohibited (see also Chokshi, Tielens & Hollenbach 1993; Dominik & Tielens 1997). As shown in Asano et al. (2014), however, the Milky Way extinction curve cannot be explained if coagulation is stopped by such a threshold. Hirashita & Voshchinnikov (2014) indeed showed that the variation of extinction curves in the Milky Way is better explained without coagulation threshold. Therefore, we assume that coagulation always occurs if two grains meet in the dense ISM.

3 APPLICATION TO A ONE-ZONE MODEL

There are some simplifications and modifications in our formulation compared with A13. Although our main purpose is to develop a model to be implemented in a hydrodynamical simulation, it is useful to check if our model produces similar grain size distributions to those found in previous models (especially A13). Our dust model requires metallicity evolution (or chemical evolution) as input. A13 developed an elaborated model for chemical enrichment by adopting detailed metal yield tables. They also used theoretical calculation results of dust condensation efficiency for AGB stars and SNe in the literature. However, as mentioned above, our formulation avoids adopting a specific dust yield table because of the uncertainty in such calculations. Therefore, it is not possible to compare our calculation with A13 under the exactly same condition. Nevertheless, since the simplification we apply should not change the model essence, our results should be similar to theirs.

We simply mimic A13's chemical enrichment model by using the following fitting formula to their results: $Z = 0.6(t/\tau_{\text{SF}}) Z_\odot$, where

---

[3]In equation (26), because of the δ function, the integration is executed under constraint $m_2 = m - m_1$. We formally adopt $\rho_{\text{d}}(m_2, t) = 0$ when $m_2 < 0$ (i.e. $m_1 > m$). Because the second term on the right-hand side in equation (26) should be symmetric by the interchange of m_1 and m_2, we can find that it is also expressed as $\frac{m}{2} \int_0^\infty \alpha(m_1, m - m_1) \rho_{\text{d}}(m_1, t) \rho_{\text{d}}(m - m_1, t) \mathrm{d}m_1$.
[4]Detailed grain charging processes could be important for coagulation if the grain motion is Brownian (thermal) (e.g. Ivlev et al. 2015). Under the density range of interest ($n_{\text{H}} \lesssim 10^3$ cm^{-3}), turbulence is unlikely to decay completely (Larson 1981). Since the grain velocities induced by turbulence are much higher than the thermal velocities, the Coulomb potential is not important for coagulation.

τ_{SF} is the star formation time-scale ($\tau_{SF} \equiv M_{gas}/\psi$, where M_{gas} the total gas mass and ψ is the star formation rate), which is assumed to be constant. This formula comes from their fig. 6, which indeed shows that the metallicity evolves roughly proportionally to the age under a constant star formation time-scale. Accordingly, we assume that the metals are supplied at a constant rate as $\dot{\rho}_Z = \rho_{gas}\dot{Z}$. We adopt $\tau_{SF} = 5$ Gyr (A13's fiducial value). Note that the metallicity evolution formula in this paragraph is just used for the one-zone model adopted in this section. We solve equation (3) but neglect the last term (i.e. $\dot{\rho}_{gas} = 0$).

Following A13's model, we separate the ISM into two phases: the cold and warm phases. We adopt $T_{gas} = 10^2$ K and $n_H = 30 \, cm^{-3}$ in the cold medium, and $T_{gas} = 10^4$ K and $n_H = 0.3 \, cm^{-3}$ in the warm medium.[5] The mass fraction of the cold phase is denoted as η_{cold}. Accordingly, the mass fraction of the warm phase is $1 - \eta_{cold}$. We consider coagulation and accretion only in the cold phase, while we calculate shattering only in the warm phase. Because the model used in this section treats a galaxy as a single-zone object, the galaxy structure cannot be taken into account. Thus, in a single time-step Δt, we calculate coagulation and accretion in $\eta_{cold}\Delta t$, while we compute shattering in $(1 - \eta_{cold})\Delta t$. We consider the other processes (stellar dust production and dust destruction by SN shocks) in the entire time-step.

For SN destruction, we assume that SNe (with progenitor mass $>8 \, M_\odot$) occur instantaneously after star formation (i.e. the lifetime of SN progenitor is zero). In this case, the SN rate γ is proportional to the star formation rate (ψ). Thus, for the ratio M_{gas}/γ appearing in equation (9), we obtain $M_{gas}/\gamma = M_{gas}/(\nu_{SN}\psi) = \tau_{SF}/\nu_{SN}$, where ν_{SN} is the proportionality constant between ψ and γ. We adopt $\nu_{SN} = 1.0 \times 10^{-2}$ based on the Chabrier (Chabrier 2003) initial mass function (i.e. we adopt $M_{gas}/\gamma = 5 \times 10^7$ yr in this section).

In Fig. 1(a), we show the time evolution of grain size distribution. This model is referred to as the standard one-zone model. We reproduce A13's evolutionary behaviour of grain size distribution as follows. The grain size distribution is dominated by stellar dust production at $t \lesssim 0.3$ Gyr; as a consequence, the grain size distribution is dominated by large ($a \sim 0.2 \, \mu m$) grains. At $t \gtrsim 0.3$ Gyr, shattering begins to produce small grains. After $t \sim 1$ Gyr, dust growth by accretion drastically increases the small grain abundance. As noted by A13, accretion has a prominent effect on small grains, which have shorter accretion time-scales than large grains (equation 13; see also Kuo & Hirashita 2012). At $t \sim 3$–10 Gyr, accretion continues to increase the small grain abundance, while coagulation pushes the grains to larger sizes. Because the increased abundance of small grains enhances shattering of large grains, the abundance of the largest grains decreases at $t \sim 3$–10 Gyr.

There are some slight differences from A13's results. At young ages ($t \lesssim 0.3$ Gyr), the peak of $a^4 n(a)$ lies around $\sim 0.5 \, \mu m$ in A13. This is due to the difference in the adopted size distribution of dust grains produced by stars, especially by SNe. However, the size distribution of dust grains formed by SNe is uncertain in the sense that it is affected by the ambient ISM density and grain species (Nozawa et al. 2007). At old ages ($t \sim 10$ Gyr), there is a prominent peak of $a^4 n(a)$ at $a \sim 0.01 \, \mu m$ in A13's result, while our model predicts a rather flat shape of $a^4 n(a)$ between $a \sim 0.001$ and $0.02 \, \mu m$. This is because we do not impose any coagulation threshold as explained in Section 2.5: in A13's model, coagulation is stopped

Figure 1. Evolution of grain size distribution for the one-zone model in Section 3. The solid, dotted, dashed, dot–dashed, and triple-dot–dashed lines represent the results at $t = 0.1$, 0.3, 1, 3, and 10 Gyr, respectively. For the vertical axis, we present the grain size distribution per hydrogen multiplied by a^4: the resulting quantity is proportional to the grain mass distribution per log a. Thus, if the value of $a^4 n(a)$ is high at a certain grain radius, it means that the mass is dominated at that grain size. Panels (a) and (b) show the standard one-zone model and the dense one-zone model, respectively. The thin line marked with 'MRN slope' in panel (b) shows the power-law slope of the MRN grain size distribution [$n(a) \propto a^{-3.5}$].

around $\sim 0.01 \, \mu m$ because larger grains have higher velocity than the threshold. Since we do not impose the threshold, coagulation occurs further in our model. However, coagulation is not strong enough to produce $0.1 \, \mu m$ grains even in our model. There is a dip around $a \sim 0.1 \, \mu m$ caused by the size gap between the coagulated grains and the stardusts, which is also seen in A13. In A13, there is another dip created by shattering at sub-micron radii, but this is simply caused by their adopted grain velocities, which have a steep increase at sub-micron sizes. This steep dependence of grain velocity on grain radius should be smoothed if we consider a variety of gas densities. As a consequence, we expect that the dip at sub-micron radii in A13 would be eliminated in reality, and that the grain size distribution approaches what we predict in this paper.

---

[5]A13 adopted $T_{gas} = 6000$ K, but we adopt this value for the pressure equilibrium with the cold medium. The difference, however, does not affect the results significantly.
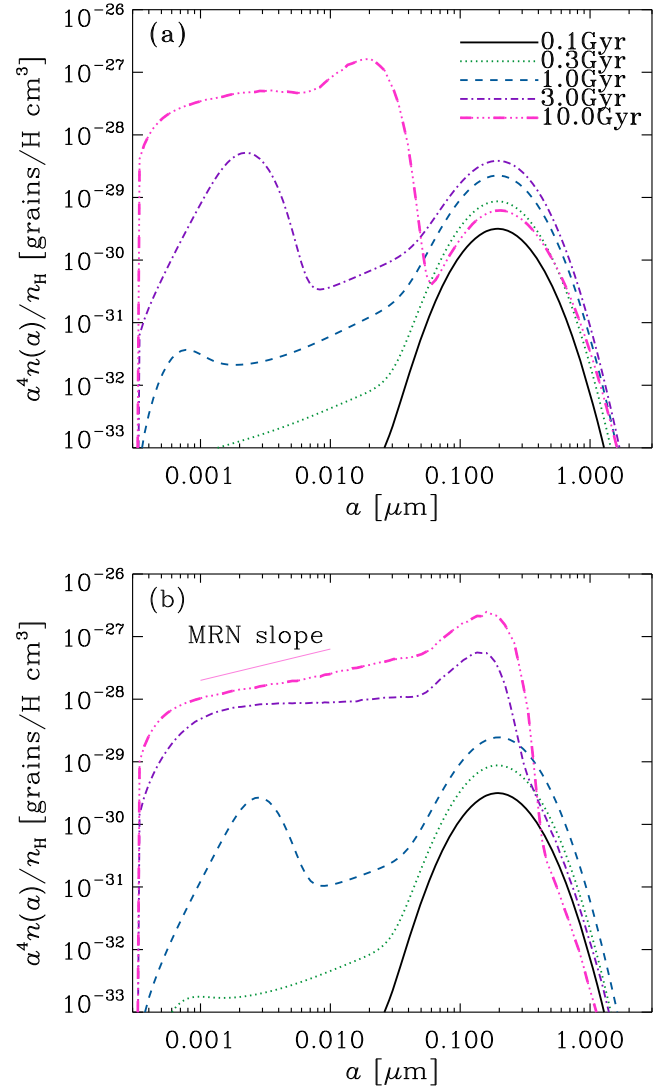
As pointed out by Nozawa et al. (2015), inclusion of a denser medium is necessary to produce the MRN-like grain size distribution that reproduces the Milky Way extinction curve. In their scenario, creation of grains with $a \sim 0.1\,\mu$m by coagulation is essential. Therefore, we examine another model in which we assume the gas density and temperature in the dense phase to be $n_{\mathrm{H}} = 300\,\mathrm{cm}^{-3}$ and $T_{\mathrm{gas}} = 25$ K (Nozawa et al. 2015).[6] This model is referred to as the dense one-zone model. In Fig. 1(b), we show the evolution of grain size distribution for the dense one-zone model. Compared with the standard one-zone model, the dense one-zone model shows quicker dust growth. At $t = 0.3$ Gyr, the two models have little difference because stellar dust production and shattering are not affected by the dense medium. At $t = 1$ Gyr, the bump at $a \sim 0.003\,\mu$m produced by accretion is higher in the dense one-zone model because the denser condition is suitable for efficient accretion. At $t = 3$–10 Gyr, the bump created by accretion is smoothed by coagulation, which produces grains even larger than $a \sim 0.1\,\mu$m. At $t = 10$ Gyr, the slope of the grain size distribution is similar to that of the MRN distribution. Interestingly, the upper cut-off of grain radius is also consistent with the value assumed in the MRN grain size distribution ($\sim 0.25\,\mu$m). Therefore, our model also confirms the conclusion by Nozawa et al. (2015), who pointed out the necessity of the dense medium (i.e. efficient accretion and coagulation) in reproducing the MRN grain size distribution.

4 APPLICATION TO A GALAXY SIMULATION

4.1 Simulation

Our development of grain size evolution model is aimed at implementation in galaxy simulations. For the first step, we here post-process the simulation of an isolated spiral galaxy in A17. We briefly review their simulation, and refer the interested reader to A17 for details.

We use the modified version of GADGET-3 N-body/SPH code (the original version was introduced by Springel 2005, and the modified version is referred to as GADGET-3-OSAKA), and our simulation includes dark matter, gas, and star particles. We install the Grackle[7] chemistry and cooling library (Bryan et al. 2014; Kim et al. 2014; Smith et al. 2017) to solve non-equilibrium primordial chemistry network for H, D, He, H_2, and HD. This allows us to compute the gas properties down to low temperatures ~ 100 K and up to higher densities $n \sim 100\,\mathrm{cm}^{-3}$. We adopt the same initial condition as used in the low-resolution model of AGORA simulations (Kim et al. 2014, 2016) (see also table 1 of A17). To 'construct' a disc galaxy, they included three components in the initial condition: halo, stellar disc, gas disc, and bulge with the total mass of each component being 1.25×10^{12}, 4.30×10^9, 8.59×10^9, and $3.44 \times 10^{10}\,\mathrm{M}_\odot$, respectively. The numbers of particles are 10^5 for the halo, stellar disc, and gas disc, and 1.25×10^4 for the bulge. We apply the minimum gravitational softening length $\varepsilon_{\mathrm{grav}} = 80$ pc and we allow the baryons to collapse to 10 per cent of this value. We find that the variable gas smoothing length reaches a minimum value of ~ 22 pc with our models of gas cooling, star formation and feedback. The

star formation is assumed to occur in a local free-fall time with an efficiency of 0.01, and the star particles are stochastically created from gas particles as described in Springel & Hernquist (2003), consistently with the SFR density. A17 only considered metal production and stellar feedback by Type II SNe according to Kim et al. (2014) and Todoroki (2014). Following Aoyama et al. (2018), we newly include the metal and dust production by Type Ia SNe and AGB stars in addition to Type II SNe. The formation of various metal elements is treated by implementing the CELIB package (Saitoh 2017), and the metals are injected according to the lifetimes of the progenitors and the metal yields (see the references in Saitoh 2017). At the same time of metal production, stellar feedback is also considered by depositing progenitor-dependent energy given by CELIB in the neighbouring gas particles. The fractions of distributed energy and metal mass among the particles are determined by the weight proportional to the SPH kernel in the same way as A17. This new implementation based on CELIB does not cause a significant difference from A17 as far as this paper is concerned.

4.2 Post-processing for dust evolution

We sample some SPH gas particles (referred to as gas particles) and investigate the dust evolution on those particles in detail. This implicitly assumes that the dust is dynamically coupled with the gas through gas drag. We choose particles in the snapshot at $t = 10$ Gyr and trace back the history of those particles. The cold/dense (warm/diffuse) ISM is defined as $n_{\mathrm{H}} > 10\,\mathrm{cm}^{-3}$ and $T_{\mathrm{gas}} < 10^3$ K ($0.1 < n_{\mathrm{H}} < 1\,\mathrm{cm}^{-3}$ and $10^3 < T_{\mathrm{gas}} < 10^4$ K), and extract 75 (77) particles for the cold/dense (warm/diffuse) phases in the following way. We ignore the particles at $R < 0.1$ kpc (R is the radius from the galaxy centre in the projection on to the disc plane), where we find a concentration of gas particles whose physical condition is not typical of the galactic disc ($n_{\mathrm{H}} > 100\,\mathrm{cm}^{-3}$ and $Z \gtrsim 3\,Z_\odot$) but could be typical of the 'galactic centre'. Thus, we choose gas particles located at $R = 0.1$–4 kpc to examine the dust evolution in a galactic disc. The outer radius, $R = 4$ kpc, is determined by the fact that we rarely find cold/dense gas particles at $R > 4$ kpc. To extract the gas contained in the disc, we also restrict the height as $-0.3 < z < 0.3$ kpc (z is the height from the galactic disc plane). To avoid selecting particles which experienced peculiar chemical enrichment not typical of the galactic disc (e.g. halo origin, galactic centre origin, etc.), we only select gas particles with $0.5 < Z < 2\,Z_\odot$ in the 10 Gyr snapshot (however, only a small number of gas particles are excluded by this metallicity criterion). Among the particles satisfying these criteria, we randomly extracted 75 and 77 particles from the cold/dense and warm/diffuse gas particles. These numbers are determined to obtain statistically robust conclusions. Direct implementation of our model to the simulation (i.e. all the gas particles) is left for future work. The extracted gas particles are shown on the phase (T_{gas}–n_{H}) diagram in Fig. 2. The 75 cold/dense and 77 warm/diffuse particles are referred to as the dense and diffuse sample, respectively.

In order to calculate the evolution of grain size distribution, we record the time evolution of gas density (n_{H}), gas temperature (T_{gas}), and metallicity (Z) for each gas particle. In addition, we also need the timing and number of SNe sweeping the gas particle for the purpose of estimating dust destruction by SNe (see below). Since the number of SNe is a discrete integer number, we count it up (N_{SN} is the cumulative number of SNe affecting the gas particle of interest; see section 2.2 of A17 for how to estimate the number of SNe on each gas particle).
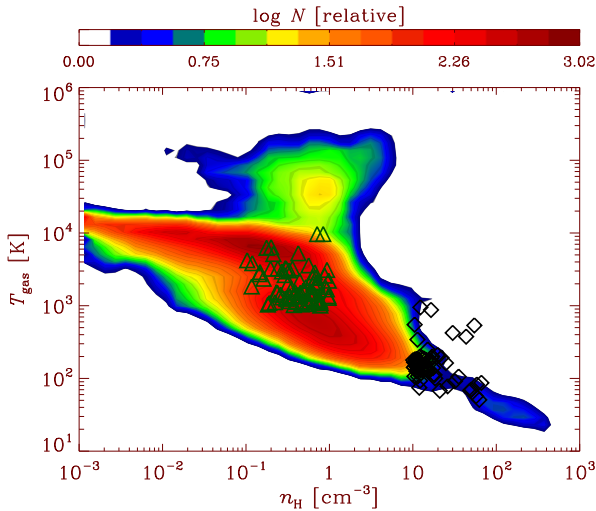
---

[6]Precisely speaking, Nozawa et al. (2015) included such a dense gas phase in addition to the above two phases. Since it is not convenient to add such a component in our code, we simplified the formulation by neglecting the component with $n_{\mathrm{H}} = 30\,\mathrm{cm}^{-3}$. This simplified treatment is sufficient for the purpose of this section.

[7]https://grackle.readthedocs.org/

Figure 2. Distribution of the sampled gas particles at $t = 10$ Gyr on the phase (T_{gas}–n_H) diagram. The green triangles and black diamonds show the 75 cold/dense and 77 warm/diffuse gas particles (dense and diffuse sample), respectively. The colour map shows the distribution of all the gas particles in the simulation at $t = 10$ Gyr. The colours correspond to the logarithmic number density of the gas particles as shown in the colour bar. Some data points located in the white region are isolated data points (the coloured region shows the area where data points are concentrated).

Using the metallicity evolution of each gas particle, we calculate $\dot{\rho}_Z = \mu m_{gas} n_{gas} \dot{Z}$, which is used to estimate the stellar dust production through equation (4). For dust destruction by SNe, we evaluate the SN rate by $\gamma = \Delta N_{SN}/\Delta t$, where ΔN_{SN} is the number of SNe hitting on the gas particle in the time interval Δt [Δt is the time-step, and $\Delta N_{SN} = N_{SN}(t + \Delta t) - N_N(t)$]. We use the mass of the gas particle for M_{gas} in equation (9).

It is generally difficult to spatially resolve dense clouds where grain growth by accretion and coagulation occurs. Thus, we adopt a subgrid model for coagulation and accretion following A17. We

'turn on' accretion and coagulation for gas particles that satisfy $n_H > 10\,\text{cm}^{-3}$ and $T_{gas} < 1000$ K. We assume that the mass fraction of f_{dense} of such a dense particle is condensed into dense clouds with $n_H = n_{H, dense} = 10^3\,\text{cm}^{-3}$ and $T_{gas} = T_{gas, dense} = 50$ K on subgrid scales and that accretion and coagulation occur only in those dense clouds.

Since shattering preferentially occurs in the diffuse ISM (Yan et al. 2004), we turn on shattering only in gas particles with $n_H < 1\,\text{cm}^{-3}$. No subgrid treatment is necessary for shattering, since the diffuse ISM is spatially resolved.

4.3 Analysis of grain size evolution

In order to show the history of the physical conditions which each gas particle experiences, we present the evolution of the relevant quantities for three randomly chosen gas particles in the dense and diffuse sample (recall that they are sampled according to the physical state at $t = 10$ Gyr) in Fig. 3. We find that the gas density and temperature fluctuate significantly regardless of the physical state at $t = 10$ Gyr. There is no systematic difference in the evolution of metallicity and SN number between the two samples. The metallicity increase correlates with the number of SNe because SNe supply metals.

We show the evolution of grain size distribution for the above three chosen gas particles in the dense sample in Fig. 4. We observe an evolutionary trend common for all the three particles and similar to the behaviour found for the one-zone models in Section 3: in the early phase, the dust is dominated by large grains produced by stars. At $t \sim 0.3$–1 Gyr, a tail develops towards the small grain size by shattering. At the later stage, accretion and coagulation drastically affect the grain size distribution: accretion increases the small grain abundance and creates a bump as noted in Section 3, while coagulation tends to deplete small grains and increase large grains. Although these evolutionary tendencies are common for all the three particles, there is a large variety in the grain size distribution, especially in the later phase, mainly because dust growth processes
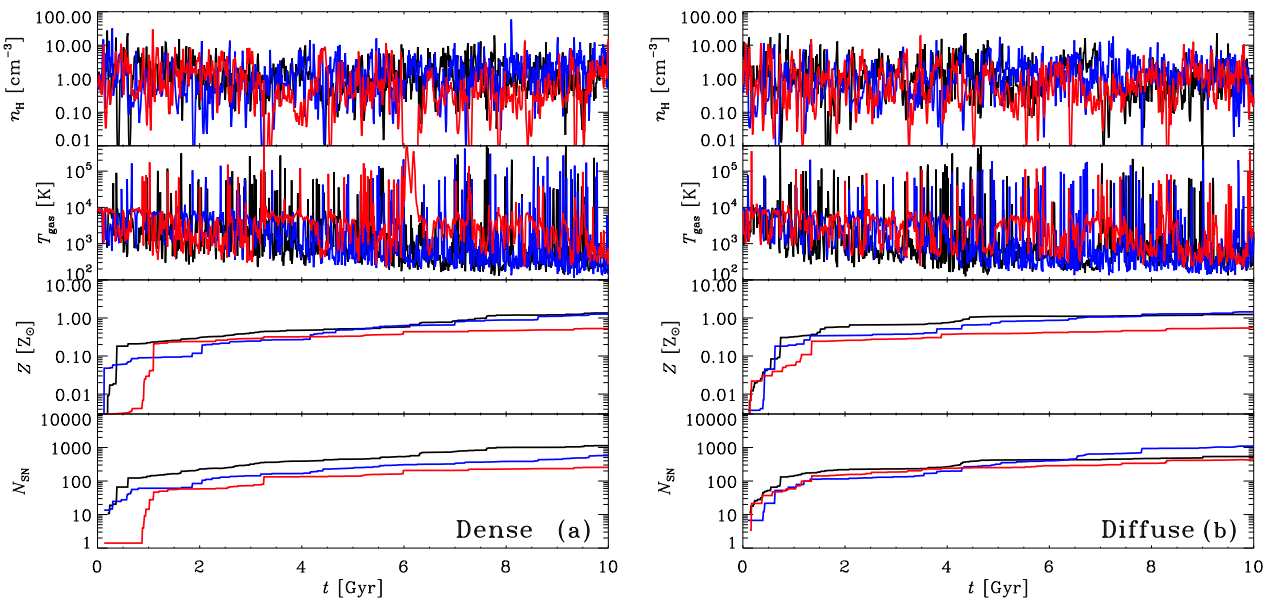
Figure 3. Time evolution of physical quantities in three randomly chosen gas particles in (a) the dense sample and (b) the diffuse sample. The different colours (black, red, and blue) show different gas particles. The quantities shown from top to bottom are the hydrogen number density, gas temperature, metallicity, and cumulative number of SNe.
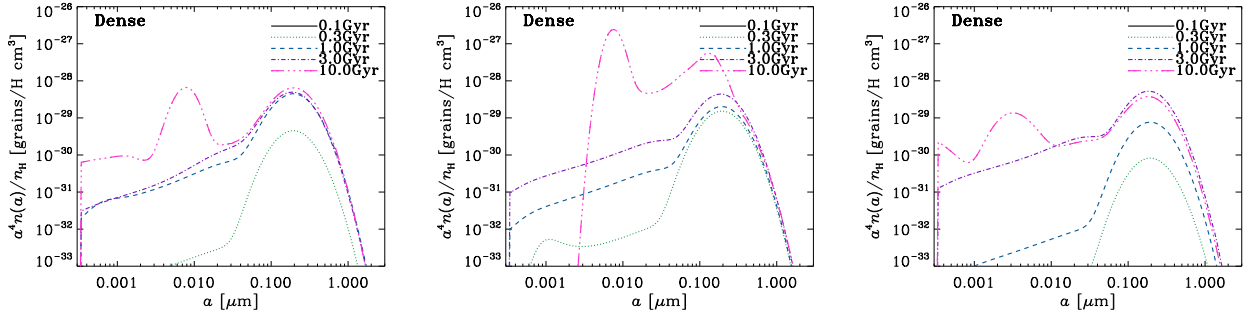
Figure 4. Grain size distributions at $t = 0.1$, 0.3, 1, 3, and 10 Gyr for the solid, dotted, dashed, dot–dashed, and triple-dot–dashed lines, respectively. The left-hand, middle, and right-hand panels show the evolution of the dense gas particles shown in black, blue, and red in Fig. 3(a), respectively.
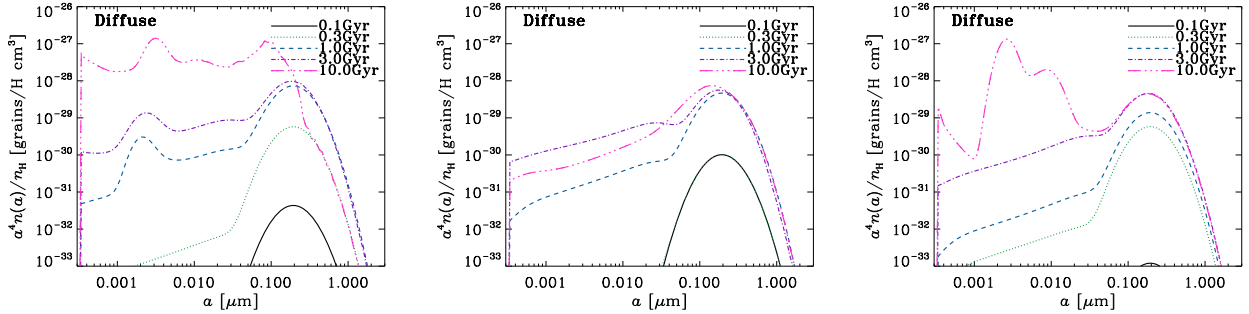

Figure 5. Same as Fig. 4 but for the diffuse gas particles shown in Fig. 3(b).

(accretion and coagulation) that dramatically impact the grain size distribution are sensitive to the history (i.e. when and how long the dust is included in the cold/dense phase).

In Fig. 5, we show the evolution of grain size distribution for the above three chosen particles in the diffuse sample. We broadly find an evolutionary trend similar to that found for the one-zone models in Section 3 and for the dense sample above, although the variety is large among the gas particles. Statistical comparison between the diffuse and dense samples is presented later. Interestingly, the second case in Fig. 5 shows that small grains are more depleted at 10 Gyr than at 3 Gyr. This is because of the destruction by SNe in the last few Gyr; indeed, this case corresponding to the blue line in Fig. 3(b) shows a larger increase in N_{SN} at $t = 7$–10 Gyr compared with the other cases.

To present the statistics property of the grain size distributions in various epochs ($t = 0.1$, 1, and 10 Gyr), we show the median and 25th and 75th percentiles in Fig. 6 (i.e. half of the particles in each sample is located in the shaded region). The grain size distributions are similar between the dense and diffuse samples at $t = 0.1$ and 1 Gyr. This is naturally expected since the physical states at such young ages do not correlate with those at $t = 10$ Gyr. At $t = 10$ Gyr, however, we do see a larger scatter in the dense sample than in the diffuse sample because of recent dust growth (accretion and coagulation) in the dense phase. As mentioned above, accretion has a dramatic effect on the small grain abundance, while coagulation tends to deplete small grains and to create large grains. Thus, the interplay between accretion and coagulation produces a large scatter in the grain size distribution both at large and small grain radii depending on the duration of dust residence in cold and dense gas. In summary, the current ISM phase affects the grain size distribution in such a way that the grain size distribution in the dense gas phase tends to have a larger variation.

The resulting grain size distributions are also compared with the MRN slope in Fig. 6. Although the dispersion is large, the grain size distribution at $t = 10$ Gyr is broadly consistent with the MRN slope in both dense and diffuse samples. The grain size distributions at $t = 0.1$ and 1 Gyr are dominated by large grains. Therefore, the interstellar processing produces MRN-like grain size distributions at $t \gtrsim 3$ Gyr, which is comparable to the age of the Milky Way.

5 DISCUSSION

In the above, we have implemented our evolution model of grain size distribution in a hydrodynamical evolution model of the ISM by post-processing. We have confirmed that the new framework reproduces the evolutionary trend of grain size distribution shown in previous work; that is, the evolution from grain size distributions dominated by large grains to MRN-like ones as a result of interstellar processing (especially interplay between accretion and coagulation). At the same time, we have also shown that there is a large dispersion in the grain size distributions especially in the later epoch ($t \gtrsim 3$ Gyr).

Although the implementation of our grain size evolution model is a successful first step, there are some observational and computational issues. Prediction of observable quantities is important for testing the model. As done by previous studies such as Hou, Hirashita & Michałowski (2016) and Hou et al. (2017), we calculate extinction curves for the purpose of comparison with observations. The computational issue, on the other hand, is related to the capability required to simultaneously solve hydrodynamics and grain size distribution. We discuss these issues in the following subsections.
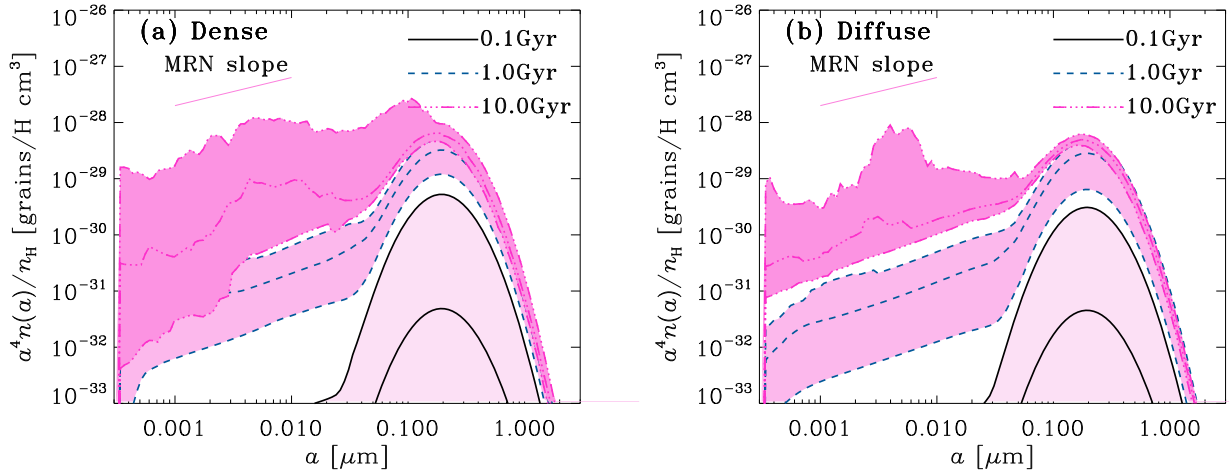
Figure 6. Variation of grain size distribution among the particles at $t = 0.1$, 1, and 10 Gyr (solid, dashed and triple-dot–dashed lines, respectively) in (a) the dense sample and (b) the diffuse sample. For each epoch, the middle line is the median and the boundaries of the shaded region shows 25th and 75th percentiles at each grain radius. For $t = 0.1$ Gyr, the lower solid line is not shown because it is located below the range of the vertical axis.

5.1 Extinction curves

Extinction curves have been useful in constraining the grain size distribution (e.g. Weingartner & Draine 2001). Here, we calculate extinction curves based on the grain size distributions obtained in Section 4. The extinction at wavelength λ in units of magnitude (A_λ) is written as

$$A_\lambda = 2.5 \log \mathrm{e} \sum_i \int_0^\infty n_i(a) \pi a^2 Q_{\mathrm{ext}}(a, \lambda), \qquad (27)$$

where $Q_{\mathrm{ext}}(a, \lambda)$ is the extinction efficiency factor, which is evaluated by using the Mie theory (Bohren & Huffman 1983) with the same optical constants for silicate and carbonaceous dust (graphite) as in Weingartner & Draine (2001). The subscript i means the grain composition (silicate and carbonaceous dust). For the first step, the mass fractions of silicate and carbonaceous dust are fixed to 0.54 and 0.46, respectively (number ratio 0.43:0.57) with the same grain size distribution (Hirashita & Yan 2009). Because this fraction is valid only for the Milky Way, we concentrate on the comparison with the Milky Way extinction curve below. For other extinction curves, we need further elaboration on the separate treatment of silicate and carbonaceous dust (Bekki, Hirashita & Tsujimoto 2015; Hou et al. 2016). We also note that there are other grain materials that could explain the Milky Way extinction curve (Zubko, Dwek & Arendt 2004; Jones et al. 2013). For simplicity, we concentrate on the above silicate–graphite model in this paper.

In Fig. 7, we show the extinction curves at $t = 1$, 3, and 10 Gyr (the extinction curves at $t < 1$ Gyr are as flat as the ones at $t = 1$ Gyr). To concentrate on the extinction curve shape, we normalize all the extinction curves to the V-band value. We show the median and 25th and 75th percentiles at each age. At $t \lesssim 1$ Gyr, the extinction curves are flat, reflecting the grain size distribution dominated by the large grains produced by stars. As the abundance of small grains increases, the extinction curve becomes steeper with more prominent 2175 Å bump created by small carbonaceous grains. Because of the large variation in the small grain abundance relative to the large grain abundance, the extinction curve shape has a large variation at UV wavelengths at $t = 10$ Gyr. As we observe in Fig. 6, the variety in the grain size distribution is large at grain radii $a \lesssim 0.05$ μm at $t = 10$ Gyr, which affects the extinction at $\lambda \lesssim 2\pi a \sim 0.3$ μm.

We also observe some difference between the dense and cold gas in the extinction curves shown in Fig. 7. As clarified in Fig. 6, the scatter in the grain size distribution is larger in the dense gas than in the diffuse gas at $t = 10$ Gyr. As a consequence, the variation in the extinction curves is larger in the dense gas than in the diffuse gas. For comparison, we show the observed Milky Way extinction curve and its variation in various lines of sight (Pei 1992; Fitzpatrick & Massa 2007; Nozawa & Fukugita 2013). It seems that the extinction curves in the simulation have a larger variety than the observed scatter. However, it is likely that the scatter of extinction curves are significantly overestimated compared with the observed variance, because an observational extinction curve represents the averaged extinction curve in a line of sight, which could contain gas with a variety of physical states. Therefore, the dispersion in the simulated extinction curves for the individual gas particles can be taken as an upper limit for the actually observed variation in extinction curves.

As we observe in Fig. 6, the median of the extinction curves at $t = 10$ Gyr is steeper in the dense gas than in the diffuse gas. In contrast, Hou et al. (2017), who represented the entire grain size range by two sizes (two-size approximation proposed by Hirashita et al. 2015) in their theoretical model, showed that the extinction curves at $t = 10$ Gyr is flatter in the dense ISM than in the diffuse ISM because of more efficient coagulation. The variation in the observed UV extinction curve slope (Fitzpatrick & Massa 2007) can also be interpreted as extinction curves being flatter in the denser ISM (Hirashita & Voshchinnikov 2014; Hou et al. 2017). This implies that our model overproduces the relative abundance of small grains to large grains in the dense gas. We make some efforts of resolving this issue in the next subsection.

The above simple model of silicate–graphite mixture may not be applied to extinction curves which do not have a clear 2175 Å bump. Pei (1992) and Weingartner & Draine (2001) argued that the extinction curves in the Large and Small Magellanic Clouds (LMC and SMC), which have a weaker or no 2175 Å bump, could be reproduced by decreasing the fraction of graphite. However, Hou et al. (2016), using their dust evolution models, showed that small carbonaceous grains are inevitably produced as a result of interstellar processing. Thus, they suggested that the extinction curves without a prominent bump can be produced either by selectively destroying small carbonaceous grains by SN destruction or by introducing
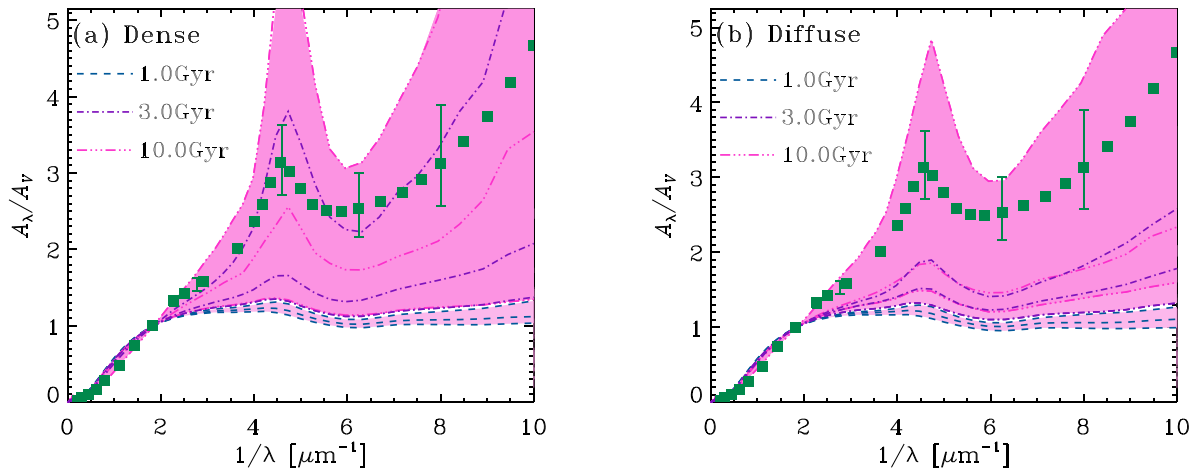
Figure 7. Variation of extinction curves among the gas particles at $t = 1$, 3, and 10 Gyr (dashed, dot–dashed, and triple-dot–dashed lines, respectively) for (a) the dense sample and (b) the diffuse sample. For each epoch, the middle line is the median at each grain size bin and the boundaries of the shaded region shows 25th and 75th percentiles at each wavelength. Most of the shaded region for $t = 3$ Gyr is located behind that for $t = 10$ Gyr. For comparison, we also show the mean observed extinction curve in the Milky Way (squares; Pei 1992) and the dispersion among various lines of sight (bars; Fitzpatrick & Massa 2007; Nozawa & Fukugita 2013).

amorphous carbon instead of graphite. Bekki et al. (2015) proposed that small carbonaceous grains are preferentially lost through radiation-driven wind during the most recent starburst in the SMC. Nozawa et al. (2015) argued that the bumpless extinction curve in a high-redshift quasar can also be explained by using amorphous carbon instead of graphite. Therefore, it seems that reproducing the LMC and SMC extinction curves contains problems not related to the evolution of grain size distribution. Further detailed modelling of carbonaceous dust is left for the future work, which could address the origin of the LMC and SMC extinction curves.

5.2 Necessity of further tuning of the subgrid models?

From the above results, there are two issues to resolve. (i) As we observe in Fig. 7, the median extinction curve at $t = 10$ Gyr is flatter than the observed Milky Way extinction curve, which indicates that small grains are underproduced in our model. (ii) As we observe in the same figure, the extinction curves in the dense gas are on average steeper than those in the diffuse gas, while the opposite trend (i.e. flatter extinction curves in denser gas) is indicated observationally. These two points indicate that we need to make the small grain production more efficient (in order to make the overall extinction curve shape steeper) but that we require more conversion from small grains to large grains in the dense gas (in order to make the extinction curves in the dense gas flatter than those in the diffuse gas).

There is a possible solution that could resolve both of the above issues simultaneously; that is, making dust growth processes in the dense ISM (accretion and coagulation) more efficient. Since the small grain production at the late evolutionary stage is dominated by accretion, increasing the accretion efficiency would help to increase the overall small grain abundance. At the same time, by increasing the coagulation efficiency, small grains could be more depleted in the dense gas than in the diffuse gas. Since both processes are regulated by the subgrid model (recall that our simulation is not capable of resolving dense clouds hosting accretion and coagulation; see Section 4.2), we tune the subgrid model in this subsection.

To make accretion and coagulation more efficient, we increase the density of subgrid dense clouds to $n_{\rm H, dense} = 10^4$ cm^{-3} (with

other parameters fixed). This subgrid model is referred to as the dense subgrid model. Recall that we originally assumed $n_{\rm H, dense} = 10^3$ cm^{-3} (Section 4.2; the original subgrid model is referred to as the standard subgrid model). Zhukovska et al. (2016) proposed that the efficiency of accretion is enhanced by the Coulomb focusing for small grains even in the medium whose density is less than 10^3 cm^{-3} (see also Zhukovska, Henning & Dobbs 2018). However, in our simulation, we are not able to address the enhancing mechanism of dust growth by accretion since the regions where accretion occurs are not spatially resolved. In other words, the essential assumption here is that the accretion efficiency is enhanced by a certain mechanism; thus, it does not matter if the accretion is enhanced by the increase of gas density or the Coulomb focusing (or any other mechanism).

In Fig. 8, we show the mean grain size distributions at $t = 0.1$, 1, and 10 Gyr with 25th and 75th percentiles (this figure is to be compared with Fig. 6) for the dense subgrid model. Coagulation produces grains as large as $a \sim 1$ μm, especially in the dense ISM. As expected, the abundance of small grains is larger in the dense subgrid model than in the standard subgrid model at $t = 10$ Gyr because of the enhanced accretion rate.

In Fig. 9, we compare the extinction curves in the two subgrid models. We only show the results at $t = 10$ Gyr, when the difference between the two subgrid models is the largest. Although the diversity in the extinction curves is not very different between the two subgrid models, the median becomes significantly steeper in the dense subgrid model than in the standard subgrid model because of the higher small-grain abundance. Moreover, it is remarkable that the median extinction curves are consistent with the observed Milky Way extinction curve both in the dense and diffuse gas. We also observe that the extinction curves are not significantly different between the diffuse and dense gas in the dense subgrid model. This means that we still fail to reproduce the observational trend of flatter extinction curves in the denser ISM. Further enhancement of coagulation might be necessary, but it may create dust grains exceeding $a = 1$ μm. Such large dust grains are not consistent with observed extinction curves (e.g. MRN). Probably, further fine-tuning of coagulation should include suppression of coagulation at $a \gtrsim 1$ μm. We do not further fine-tune the model in this paper because it is
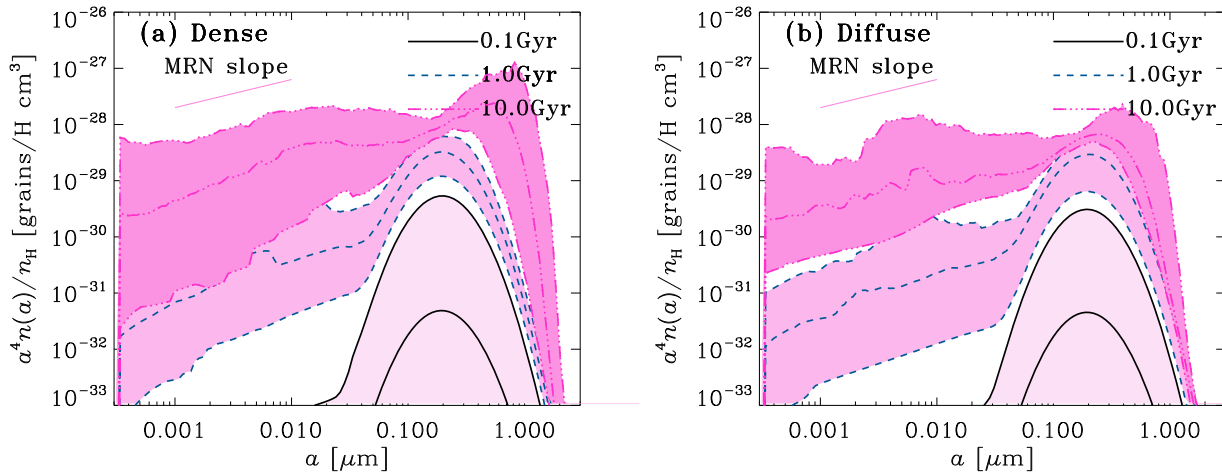
Figure 8. Same as Fig. 6 but for the dense subgrid model (Section 5.2).
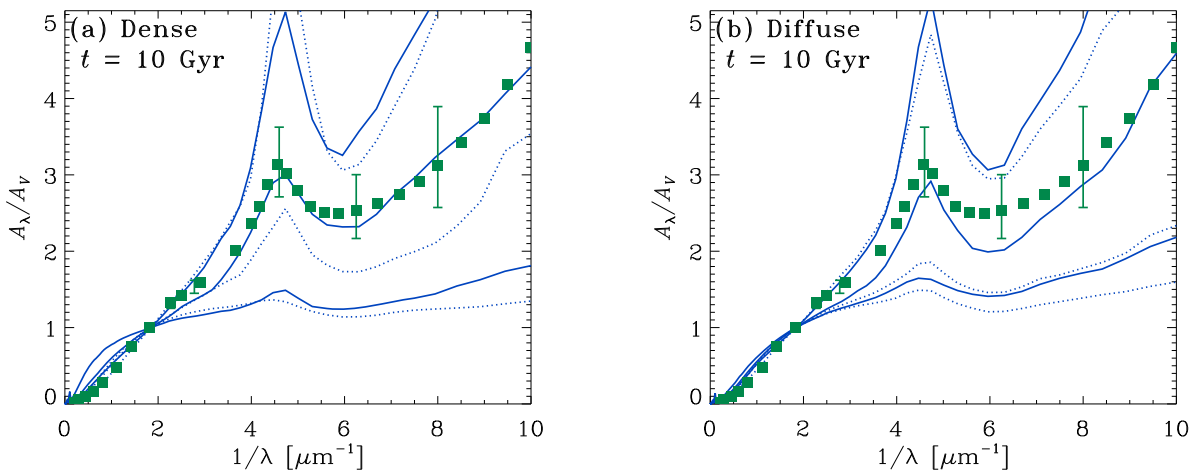

Figure 9. Variation of extinction curves at $t = 10$ Gyr. The solid and dotted lines show the results for the dense subgrid model (Section 5.2) and the standard subgrid model (i.e. the same model as shown in Fig. 7), respectively. The middle line is the median while the upper and lower lines show 25th and 75th percentiles, respectively.

not physically meaningful to complicate the subgrid model further without strong physical motivation.

It is worth emphasizing that the dense subgrid model – a simple modification of the subgrid model – reproduces the Milky Way extinction curve. Therefore, our model, combined with the hydrodynamical evolution of a Milky Way-like disc galaxy, is a useful tool, based on which we are able to investigate the evolution of grain size distribution in the entire history of galaxy evolution.

5.3 Effects of the number of grain-radius bins

Calculation of grain size distribution is computing-resource-consuming when implemented in a hydrodynamical simulation. Thus, it is interesting to investigate the effect of a reduced grain radius bin number on the calculated grain size distribution. We utilize the one-zone model used in Section 3 for this test to trace a representative grain size distribution in a galaxy. McKinnon et al. (2018) performed a test calculation for an isolated disc galaxy and adopted a bin number of $N = 16$ (although we note that they developed a second-order scheme, while ours is a first-order one). We compare the results with $N = 16$ and those with $N = 128$ (the num-

ber of bins adopted in all the above calculations) using the scheme developed in this paper.

In Fig. 10, we show the grain size distribution at various ages for $N = 16$ and 128. We observe that the lower resolution run broadly captures the shape of grain size distribution. However, there is a large difference in the bump structure at $t = 1$ Gyr in terms of both the width and the peak position. This is caused by the numerical diffusion which is unavoidable in our simple discretization method (especially for accretion, which is treated by an advection equation in the grain radius space; see Appendix B). Since the evolution of grain size distribution occurs quickly at $t \sim 1$ Gyr, the shape of the grain size distribution is sensitive to the slight change in the grain size distribution. However, at $t = 3$ and 10 Gyr, when the evolution of grain size distribution becomes more moderate than at $t \sim 1$ Gyr, the low-resolution run produces similar grain size distributions to the high-resolution run.

In order to show the effect of grain radius resolution on the prediction of dust optical properties, we compare the calculated extinction curves in Fig. 10. We find that both resolutions predict similar extinction curve shapes within ∼10 per cent of difference at the early ($t \leq 0.3$ Gyr) and late ($t \sim 10$ Gyr) phases. However, the extinction curve strongly depends on the grain radius resolution at
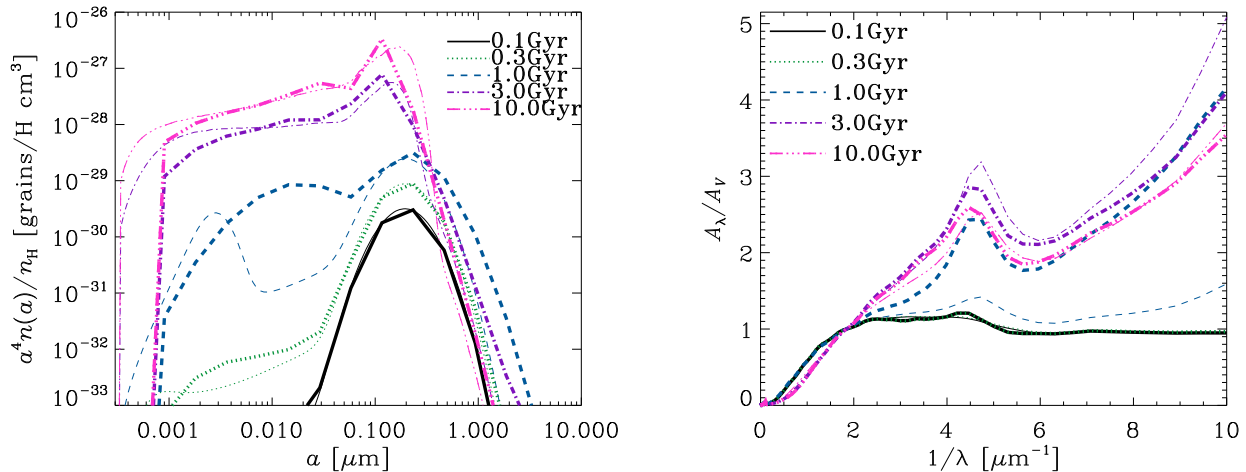
Figure 10. Comparison between the calculations with different grain radius resolutions ($N = 16$ and 128). The thick and thin lines show the calculations with $N = 16$ and 128, respectively. The solid, dotted, dashed, dot–dashed, triple-dot–dashed lines show the results at $t = 0.1, 0.3, 1, 3,$ and 10 Gyr, respectively. *Left*: Evolution of grain size distribution for the dense one-zone model (i.e. the same model as presented in Section 3 and Fig. 1b). *Right*: Extinction curves corresponding to the size distributions in the left-hand panel.

$t \sim 1$ Gyr as a result of the different bump shapes in the grain size distribution. Therefore, in the epoch when the small grain abundance rapidly evolves by accretion, the extinction curve shape is sensitive to the grain radius resolution.

In summary, the grain size distribution and the extinction curve are reasonably reproduced with a low grain radius resolution ($N \sim 16$) except in the phase of rapid dust growth by accretion. When the grain size distribution is strongly modified by accretion, the calculated grain size distribution and extinction curve strongly depend on the grain size resolution. However, in spatially resolved hydrodynamical simulations, grain growth by accretion does not occur simultaneously in all places; thus, a strong bump at a certain grain size is not expected if we average the grain size distribution over the entire galaxy or over a certain area of interest. Therefore, we expect that a low grain radius resolution with $N \sim 16$ is still useful to capture the overall shapes of grain size distribution and extinction curve, considering that calculation with a larger N is computationally expensive.

5.4 Future prospect

In this paper, we post-processed the hydrodynamical simulation of an isolated galaxy. However, if dust grains affect the gas dynamics and/or chemical properties (Bekki 2015), it is essential to solve hydrodynamics and dust evolution simultaneously. Moreover, once we implement the grain size evolution in a hydrodynamical simulation, we naturally predict, for example, the spatial variation of grain size distribution. Therefore, it is desirable to include the evolutionary scheme of grain size distribution developed in this paper in a hydrodynamical simulation.

McKinnon et al. (2018) have already implemented the evolution of grain size distribution in a hydrodynamical simulation of an isolated galaxy. Although some important processes in galaxy evolution (especially stellar feedback) are still to be included, they have succeeded in showing that the grain size distribution is strongly influenced by interstellar processing such as shattering and accretion. Their scheme has some advantages over ours. First, they treated the grains and gas as separate fluids (i.e. allowed to move with different speeds) but coupled through drag. Secondly, they considered the variation of the slope of grain size distribution within each

single grain radius bin to obtain a second-order precision. In their calculation, though, saving calculation time still seems to be an issue for galaxy-scale calculations in their section 5 (e.g. they used the first-order scheme in the end). In this respect, our formulation could be useful because of some simplifications in the treatments of sputtering, grain velocities, etc. (Section 2).

The evolution model of grain size distribution developed in this paper is also useful by itself. As shown in Section 3, the application to a one-zone model could be useful to investigate in detail how each process affects the grain size distribution. Although Asano et al. (2013) already applied their evolution model of grain size distribution to a one-zone galaxy evolution model, it would be interesting to expand the application to different types of galaxies at various redshifts. Since galaxies have a huge diversity in star formation histories, our model developed in this paper will provide a useful tool to investigate the grain size distributions in a variety of galaxies found by sensitive observational facilities such as ALMA.

6 CONCLUSION

We consider the evolution model of grain size distribution in the ISM of a galaxy. To make the implementation in hydrodynamical simulations easier, we simplify the previous model in such a way that some model-dependent assumptions on dust yield, interstellar processing, and grain velocities are replaced with simpler functional forms. For the first test of the developed framework, we apply it to a one-zone chemical evolution model of a galaxy, confirming that our new model satisfactorily reproduces the evolutionary trend of grain size distribution shown in previous work (e.g. A13): The dust abundance is dominated by large grains at $t \lesssim 0.3$–1 Gyr, while the tail towards small grain radii develops by shattering. After that, once the metallicity becomes high enough for dust growth by accretion to be efficient enough, accretion creates a bump at small grain radius ($a \sim 0.001$–0.01 μm) in the grain size distribution. This bump is pushed towards larger grain radii and smoothed by coagulation. We also confirm that efficient grain growth by coagulation and accretion in the dense ISM is essential in reproducing the so-called MRN grain size distribution, which is appropriate for the Milky Way dust.

In order to test if our model can be treated together with the hydrodynamical evolution of the ISM, we post-process a

hydrodynamical simulation of an isolated disc galaxy using the new grain evolution model. We sampled ∼80 gas (SPH) particles for each phase (dense/cold and diffuse/warm phase) based on the physical state at $t = 10$ Gyr. According to all the history of physical conditions (gas density, temperature, and metallicity) as well as the number of SN shocks, we calculate the evolution of grain size distribution for each gas particle. As a consequence of this post-processing, we find that, although the overall evolutionary behaviour of grain size distribution is similar to the results in the above one-zone model, there is a large variety in the grain size distribution among the gas particles, especially at $t \gtrsim 1$ Gyr, mainly because dust growth processes (accretion and coagulation) that dramatically impact the grain size distribution are sensitive to when and how long the dust is included in the cold/dense phase. The dispersion of the grain size distribution at $t = 10$ Gyr is larger in the dense gas than in the diffuse gas, because of the recent dust growth (accretion and coagulation) in the dense phase.

For an observational test, we calculate extinction curves based on the grain size distributions computed above. At $t \lesssim 1$ Gyr, the extinction curves are flat because the grain size distribution is dominated by large (sub-micron-sized) grains produced by stars. To reproduce the Milky Way extinction curve, the processes in the dense ISM (i.e. accretion and coagulation) play a central role. If these processes are efficient enough as we assumed in the dense subgrid model in Section 5.2, the median extinction curves are consistent with the Milky Way extinction curve in both dense and diffuse gas.

Finally, we examine the effect of degraded grain radius resolution, considering the limitation in computational resources. We show that a calculation with a small number of grain radius bins ($N \sim 16$) is still able to capture the overall shape of grain size distribution and extinction curve except in the phase of rapid dust growth by accretion, which happens around $t \sim 1$ Gyr in our simulation. However, we expect that, since all hydrodynamical elements in a galaxy do not coherently experience this dust growth phase, we still expect that a low grain radius resolution with $N \sim 16$ is useful when we are interested in averaged dust properties in a certain area.

REFERENCES

Aoyama S., Hou K.-C., Shimizu I., Hirashita H., Todoroki K., Choi J.-H., Nagamine K., 2017, MNRAS, 466, 105
Aoyama S., Hou K.-C., Hirashita H., Nagamine K., Shimizu I., 2018, MNRAS, 478, 4905
Asano R. S., Takeuchi T. T., Hirashita H., Nozawa T., 2013, MNRAS, 432, 637
Asano R. S., Takeuchi T. T., Hirashita H., Nozawa T., 2014, MNRAS, 440, 134
Bekki K., 2013, MNRAS, 432, 2298
Bekki K., 2015, MNRAS, 449, 1625
Bekki K., Hirashita H., Tsujimoto T., 2015, ApJ, 810, 39
Bianchi S., Schneider R., 2007, MNRAS, 378, 973
Bohren C. F., Huffman D. R., 1983, Absorption and Scattering of Light by Small Particles. Wiley, New York
Bryan G. L. et al., 2014, ApJS, 211, 19
Cazaux S., Tielens A. G. G. M., 2004, ApJ, 604, 222
Chabrier G., 2003, PASP, 115, 763
Chen L.-H., Hirashita H., Hou K.-C., Aoyama S., Shimizu I., Nagamine K., 2018, MNRAS, 474, 1545
Cherchneff I., Dwek E., 2010, ApJ, 713, 1
Chokshi A., Tielens A. G. G. M., Hollenbach D., 1993, ApJ, 407, 806
Dayal P., Hirashita H., Ferrara A., 2010, MNRAS, 403, 620
Dell'Agli F., García-Hernández D. A., Schneider R., Ventura P., La Franca F., Valiante R., Marini E., Di Criscienzo M., 2017, MNRAS, 467, 4431
Dominik C., Tielens A. G. G. M., 1997, ApJ, 480, 647
Draine B. T., Salpeter E. E., 1979, ApJ, 231, 77
Dwek E., 1998, ApJ, 501, 643
Ferrarotti A. S., Gail H.-P., 2006, A&A, 447, 553
Fitzpatrick E. L., Massa D., 2007, ApJ, 663, 320
Ginolfi M., Graziani L., Schneider R., Marassi S., Valiante R., Dell'Agli F., Ventura P., Hunt L. K., 2018, MNRAS, 473, 4538
Gjergo E., Granato G. L., Murante G., Ragone-Figueroa C., Tornatore L., Borgani S., 2018, MNRAS, 479, 2588
Gould R. J., Salpeter E. E., 1963, ApJ, 138, 393
Grassi T., Krstic P., Merlin E., Buonomo U., Piovan L., Chiosi C., 2011, A&A, 533, A123
Guillet V., Pineau Des Forêts G., Jones A. P., 2011, A&A, 527, A123
Harada N., Hasegawa Y., Aikawa Y., Hirashita H., Liu H. B., Hirano N., 2017, ApJ, 837, 78
Hirashita H., 2012, MNRAS, 422, 1263
Hirashita H., Ferrara A., 2002, MNRAS, 337, 921
Hirashita H., Kobayashi H., 2013, Earth Planets Space, 65, 1083
Hirashita H., Li Z.-Y., 2013, MNRAS, 434, L70
Hirashita H., Voshchinnikov N. V., 2014, MNRAS, 437, 1636
Hirashita H., Yan H., 2009, MNRAS, 394, 1061
Hirashita H., Nozawa T., Villaume A., Srinivasan S., 2015, MNRAS, 454, 1620
Hou K.-C., Hirashita H., Michałowski M. J., 2016, PASJ, 68, 94
Hou K.-C., Hirashita H., Nagamine K., Aoyama S., Shimizu I., 2017, MNRAS, 469, 870
Inoue A. K., 2011, Earth Planets Space, 63, 1027
Ivlev A. V., Padovani M., Galli D., Caselli P., 2015, ApJ, 812, 135
Jones A. P., Tielens A. G. G. M., Hollenbach D. J., McKee C. F., 1994, ApJ, 433, 797
Jones A. P., Tielens A. G. G. M., Hollenbach D. J., 1996, ApJ, 469, 740
Jones A. P., Fanciullo L., Köhler M., Verstraete L., Guillet V., Bocchio M., Ysard N., 2013, A&A, 558, A62
Kim J.-h. et al., 2014, ApJS, 210, 14
Kim J.-h. et al., 2016, ApJ, 833, 202
Kobayashi H., Tanaka H., 2010, Icarus, 206, 735
Kozasa T., Hasegawa H., Nomoto K., 1989, ApJ, 344, 325
Kuo T.-M., Hirashita H., 2012, MNRAS, 424, L34
Kuo T.-M., Hirashita H., Zafar T., 2013, MNRAS, 436, 1238
Larson R. B., 1981, MNRAS, 194, 809
Leitch-Devlin M. A., Williams D. A., 1985, MNRAS, 213, 295
Mancini M., Schneider R., Graziani L., Valiante R., Dayal P., Maio U., Ciardi B., Hunt L. K., 2015, MNRAS, 451, L70
Mathis J. S., Rumpl W., Nordsieck K. H., 1977, ApJ, 217, 425
Mattsson L., 2016, Planet. Space Sci., 133, 107
McKee C., 1989, in Allamandola L. J., Tielens A. G. G. M., eds, IAU Symp. Vol. 135, Interstellar Dust. Kluwer, Dordrecht, p. 431
McKee C. F., Hollenbach D. J., Seab G. C., Tielens A. G. G. M., 1987, ApJ, 318, 674
McKinnon R., Torrey P., Vogelsberger M., 2016, MNRAS, 457, 3775
McKinnon R., Torrey P., Vogelsberger M., Hayward C. C., Marinacci F., 2017, MNRAS, 468, 1505

McKinnon R., Vogelsberger M., Torrey P., Marinacci F., Kannan R., 2018, MNRAS, 478, 2851

Ménard B., Fukugita M., 2012, ApJ, 754, 116

Nozawa T., Fukugita M., 2013, ApJ, 770, 27

Nozawa T., Kozasa T., Umeda H., Maeda K., Nomoto K., 2003, ApJ, 598, 785

Nozawa T., Kozasa T., Habe A., 2006, ApJ, 648, 435

Nozawa T., Kozasa T., Habe A., Dwek E., Umeda H., Tominaga N., Maeda K., Nomoto K., 2007, ApJ, 666, 955

Nozawa T., Asano R. S., Hirashita H., Takeuchi T. T., 2015, MNRAS, 447, L16

Omukai K., Tsuribe T., Schneider R., Ferrara A., 2005, ApJ, 626, 627

Ormel C. W., Paszun D., Dominik C., Tielens A. G. G. M., 2009, A&A, 502, 845

Pei Y. C., 1992, ApJ, 395, 130

Popping G., Somerville R. S., Galametz M., 2017, MNRAS, 471, 3152

Saitoh T. R., 2017, AJ, 153, 85

Schneider R., Omukai K., Inoue A. K., Ferrara A., 2006, MNRAS, 369, 1437

Smith B. D. et al., 2017, MNRAS, 466, 2217

Springel V., 2005, MNRAS, 364, 1105

Springel V., Hernquist L., 2003, MNRAS, 339, 289

Takeuchi T. T., Ishii T. T., Nozawa T., Kozasa T., Hirashita H., 2005, MNRAS, 362, 592

Tielens A. G. G. M., McKee C. F., Seab C. G., Hollenbach D. J., 1994, ApJ, 431, 321

Todini P., Ferrara A., 2001, MNRAS, 325, 726

Todoroki K., 2014, Master's thesis, Univ. Nevada

Valiante R., Schneider R., Bianchi S., Andersen A. C., 2009, MNRAS, 397, 1661

Valiante R., Schneider R., Salvadori S., Bianchi S., 2011, MNRAS, 416, 1916

Ventura P., Dell'Agli F., Schneider R., Di Criscienzo M., Rossi C., La Franca F., Gallerani S., Valiante R., 2014, MNRAS, 439, 977

Weingartner J. C., Draine B. T., 2001, ApJ, 548, 296

Yajima H., Nagamine K., Thompson R., Choi J.-H., 2014, MNRAS, 439, 3073

Yamasawa D., Habe A., Kozasa T., Nozawa T., Hirashita H., Umeda H., Nomoto K., 2011, ApJ, 735, 44

Yan H., Lazarian A., Draine B. T., 2004, ApJ, 616, 895

Yasuda Y., Kozasa T., 2012, ApJ, 745, 159

Zhukovska S., Gail H.-P., Trieloff M., 2008, A&A, 479, 453

Zhukovska S., Dobbs C., Jenkins E. B., Klessen R. S., 2016, ApJ, 831, 147

Zhukovska S., Henning T., Dobbs C., 2018, ApJ, 857, 94

Zu Y., Weinberg D. H., Davé R., Fardal M., Katz N., Kereš D., Oppenheimer B. D., 2011, MNRAS, 412, 1059

Zubko V., Dwek E., Arendt R. G., 2004, ApJS, 152, 211

APPENDIX A: EQUATIONS FOR SPUTTERING AND ACCRETION

The common feature for sputtering and accretion is that these processes conserve the total number of dust grains except at the minimum grain radius below which the material should be treated as molecules rather than dust. Therefore, the following continuity equation for the grain size distribution holds for sputtering and accretion:

$$\frac{\partial n(a,\,t)}{\partial t} + \frac{\partial}{\partial a}[\dot{a}n(a,\,t)] = 0. \tag{A1}$$

The grain size distribution $n(a,\,t)$ is related to the mass distribution function $\rho_d(m,\,t)$ in the following way (see equation 1):

$$\rho_d = \frac{1}{3}an. \tag{A2}$$

Using this and $\dot{m} = 4\pi a^2 s\dot{a}$, and $\partial/\partial m = [1/(4\pi a^2 s)]\partial/\partial a$, we obtain

$$\frac{\partial \rho_d(m,\,t)}{\partial t} + \frac{\partial}{\partial m}[\dot{m}\rho_d(m,\,t)] = \dot{a}n = \frac{\dot{m}}{m}\rho_d(m,\,t). \tag{A3}$$

Furthermore, by introducing a new variable $\mu \equiv \ln m$, we obtain

$$\frac{\partial \rho_d(\mu,\,t)}{\partial t} + \frac{\partial}{\partial \mu}[\dot{\mu}\rho_d(\mu,\,t)] = 0. \tag{A4}$$

In deriving this equation, we used $\dot{\mu} = \dot{m}/m$ and $dm/d\mu = m$. Equation (A4) is useful, since we often adopt grids with a logarithmically equal width in numerical calculations. It is interesting to point out that ρ_d is expressed in a complete conservative form for accretion and sputtering if we use a logarithmic grid.

APPENDIX B: DISCRETE FORMS

For the reader's convenience, we explicitly write the discretized form for each process. For numerical calculation, we consider N discrete grain radii, and denote the lower and upper bounds of the ith ($i = 1, \cdots, N$) bin as $a_{i-1}^{(b)}$ and $a_i^{(b)}$, respectively. We adopt $a_i^{(b)} = a_{i-1}^{(b)}\delta$, $a_0^{(b)} = a_l$, and $a_N^{(b)} = a_u$ with $\log \delta = (1/N)\log(a_u/a_l)$. We represent the grain radius and mass in the ith bin with $a_i \equiv (a_{i-1}^{(b)} + a_i^{(b)})/2$ and $m_i \equiv (4\pi/3)a_i^3 s$. The boundary of the mass bin is defined as $m_i^{(b)} \equiv (4\pi/3)[a_i^{(b)}]^3 s$. The interval of logarithmic mass grids is denoted as $\Delta\mu = 3\delta$. We also discretize the time and determine the time-step according to Section B4. We adopt $N = 128$, $a_l = 3 \times 10^{-4}$ μm, and $a_u = 10$ μm. We apply $n(a_0,\,t) = n(a_N,\,t) = 0$ for the boundary condition.

We denote the value of quantity Q at a discrete grid as Q_i^n, where i and n specify the grain size and time, respectively.

B1 Sputtering and accretion

We obtain the following equation as a discrete form of equation (A4) with time and grid widths of Δt and $\Delta\mu$, respectively:

$$\frac{\rho_{d,i}^{n+1} - \rho_{d,i}^n}{\Delta t} + \frac{\dot{\mu}_i^n \rho_{d,i}^n - \dot{\mu}_{i-1}^n \rho_{d,i-1}^n}{\Delta\mu} = 0 \tag{B1}$$

or

$$\frac{\rho_{d,i}^{n+1} - \rho_{d,i}^n}{\Delta t} + \frac{\dot{\mu}_{i+1}^n \rho_{d,i+1}^n - \dot{\mu}_i^n \rho_{d,i}^n}{\Delta\mu} = 0. \tag{B2}$$

To obtain physically reasonable results, it is desirable to adopt upwind differencing. Therefore, we use the first equation for accretion, which always increases the grain mass, while we apply the second for sputtering, which always decreases the grain mass. Accordingly, we obtain

$$\rho_{d,i}^{n+1} = \rho_{d,i}^n - \frac{\Delta t}{\Delta\mu}(\dot{\mu}_i^n \rho_{d,i}^n - \dot{\mu}_{i-1}^n \rho_{d,i-1}^n) \tag{B3}$$

for accretion, and

$$\rho_{d,i}^{n+1} = \rho_{d,i}^n - \frac{\Delta t}{\Delta\mu}(\dot{\mu}_{i+1}^n \rho_{d,i+1}^n - \dot{\mu}_i^n \rho_{d,i}^n) \tag{B4}$$

for sputtering.

B2 Shattering

The mass density of grains contained in the ith bin, $\tilde{\mathcal{M}}_i^n$ is defined as $\tilde{\mathcal{M}}_i^n \equiv \rho_i^n m_i \Delta\mu$. The time evolution of $\tilde{\mathcal{M}}_i$ by shattering can be

written after discretizing equation (14) as

$$\frac{\tilde{\mathcal{M}}_i^{n+1} - \tilde{\mathcal{M}}_i^n}{\Delta t} = -m_i \tilde{\mathcal{M}}_i^{n+1} \sum_{\ell=1}^{N} \alpha_{\ell i} \tilde{\mathcal{M}}_\ell^n$$

$$+ \sum_{j=1}^{N} \sum_{\ell=1}^{N} \alpha_{\ell j} \tilde{\mathcal{M}}_\ell^n \tilde{\mathcal{M}}_j^n m_{\text{shat}}^{\ell j}(i), \tag{B5}$$

and

$$\alpha_{\ell j} = \frac{\sigma_{\ell j} v_{\ell j}}{m_\ell m_j}, \tag{B6}$$

where $m_{\text{shat}}^{\ell j}(i)$ is the total mass of the shattered fragments of a grain in the ℓth bin that enter the ith bin in the collision with a grain in the jth bin, and $\sigma_{\ell j}$ and $v_{\ell j}$ are, respectively, the grain–grain collisional cross-section and the relative collision speed between grains in bins ℓ and j. The cross-section for shattering is $\sigma_{\ell j} = \pi(a_\ell + a_j)^2$ (see equation 16). The total fragment mass in the ith bin is determined by

$$m_{\text{shat}}^{\ell j}(i) = \int_i \mu_{\text{frag}}(m; m_\ell, m_j) \, dm, \tag{B7}$$

where the fragment mass distribution μ_{frag} is given in equation (25) and the integration is executed in the radius range of the ith bin. The fragments whose radii are smaller than a_1 are removed from the calculation. In equation (B5), the first term on the right-hand side adopt a semi-implicit method; that is, we evaluate $\tilde{\mathcal{M}}_i$ at the new time-step $(n + 1)$. This stabilizes the calculation. As a consequence, we obtain

$$\tilde{\mathcal{M}}_i^{n+1} = \tilde{\mathcal{M}}_i^n/(1 + \mathcal{S}_i) + \Delta t(\text{Second Term})/(1 + \mathcal{S}_i), \tag{B8}$$

where

$$\mathcal{S}_i \equiv m_i \Delta t \sum_{\ell=1}^{N} \alpha_{\ell i} \tilde{\mathcal{M}}_\ell^n, \tag{B9}$$

and 'Second Term' is the second term on the right-hand side in equation (B5). After updating the grain size distribution for the first term, we calculate the second term.

The important aspect of shattering is that it conserves the total dust mass (if we also count the dust grains that have been removed because of $a < a_1$). Therefore, we modify the above formulation to guarantee the mass conservation as follows. We define

$$\mathcal{S}_{i,\ell} \equiv m_i \Delta t \alpha_{\ell i} \tilde{\mathcal{M}}_\ell^n, \tag{B10}$$

so that $\mathcal{S}_i = \sum_{\ell=1}^{N} \mathcal{S}_{i,\ell}$. We aim at guaranteeing the mass conservation in each treatment of grain collisions between a pair of grain radius bins (the ith and ℓth bins in the case above). Let us consider the collision between grains in the ith and ℓth bins. We temporarily renew the value in the ith bin as

$$\tilde{\mathcal{M}}_{i,\ell}^{n+i/N} = \frac{\tilde{\mathcal{M}}_{i,\ell-1}^{n+i/N}}{1 + \mathcal{S}_{i,\ell}}, \tag{B11}$$

where we formally write $\tilde{\mathcal{M}}_{i,0}^{n+i/N} = \tilde{\mathcal{M}}_i^{n+(i-1)/N}$ and $\tilde{\mathcal{M}}_i^{n+0/N} = \tilde{\mathcal{M}}_i^n$ so that this equation is valid for $\ell = 1$ and $(\ell, n) = (1, 1)$. This converges to the first term on the right-hand side of equation (B8) after all the N loops ($\ell = 1, \ldots, N$) if $\Delta t \to 0$. Immediately after equation (B11), we update the values in all bins ($1 \leq j \leq N$) as

$$\tilde{\mathcal{M}}_{j,\ell}^{n+i/N} = \tilde{\mathcal{M}}_{j,\ell-1}^{n+i/N} + \frac{\mathcal{S}_{i,\ell}}{1 + \mathcal{S}_{i,\ell}} \frac{m_{\text{shat}}^{i\ell}(j)}{m_i}. \tag{B12}$$

Noting that $\sum_{j=0}^{N} m_{\text{shat}}^{i\ell}(j) = m_i$, we find that the total dust mass is conserved if we calculate the pair of equations (B11) and (B12). We

repeat equations (B11) and (B12) for $\ell = 1, \ldots, N$ (i.e. we consider the collisions with grains in all the grain radius bins). The results after this loop is denoted as

$$\tilde{\mathcal{M}}_i^{n+i/N} = \tilde{\mathcal{M}}_{i,N}^{n+i/N}. \tag{B13}$$

We also repeat the loop for all i ($i = 1, \ldots, N$). we obtain the values for all bins (i) at the $(n + 1)$th time-step as

$$\tilde{\mathcal{M}}_i^{n+1} = \tilde{\mathcal{M}}_i^{n+N/N}. \tag{B14}$$

B3 Coagulation

We use the same procedure as shattering in calculating coagulation except that we replace $m_{\text{shat}}^{\ell j}$ with the coagulated mass $m_{\text{coag}}^{\ell j}(i)$, which is determined as follows: $m_{\text{coag}}^{\ell j}(i) = m_\ell$ if $m_{i-1}^{(b)} \leq m_\ell + m_j < m_i^{(b)}$;[8] otherwise $m_{\text{coag}}^{\ell j}(i) = 0$. The cross-section for the coagulation is $\sigma_{\ell j} = \pi(a_\ell + a_j)^2$ (see equation 16 with $\beta = 1$).

B4 Time-step

The time-step interval Δt is determined for each step as follows. For accretion and sputtering, since $\dot{a}$ is constant, the shortest time-scale of grain size change $a/\dot{a}$ is realized at the smallest radius bin. Therefore, we adopt $\epsilon_\Delta \Delta\mu/\mu$ at the smallest bin (with $\epsilon_\Delta = 0.3$), denoted as $\Delta t_{\text{acc}} = \epsilon_\Delta (\Delta\mu/\dot{\mu})_{\text{acc}}|_0^n$ and $\Delta t_{\text{sput}} = \epsilon_\Delta (\Delta\mu/\dot{\mu})_{\text{sput}}|_0^n$, for accretion and sputtering, respectively. For shattering and coagulation, we do not know in advance at which bin the processes have the shortest time-scale. It is possible to find Δt such that Δt is shorter than the inverse of the mass changing rate in all bins. However, this iterative process is time-consuming. To avoid the iteration, we introduce the following collision time-scale, τ_{coll}, which can be calculated in an independent manner from the actual shattering and coagulation calculations:

$$\tau_{\text{coll}} = 5 \times 10^7 n_{\text{H}} \left(\frac{a}{0.1 \, \mu\text{m}} \right) \left(\frac{\mathcal{D}}{0.01} \right)^{-1} \left(\frac{v_{\text{gr}}(a)}{10 \, \text{km s}^{-1}} \right)^{-1} \text{yr}, \tag{B15}$$

where $\mathcal{D} \equiv \rho_{\text{d,tot}}/(\mu m_{\text{H}} n_{\text{H}})$ is the dust-to-gas ratio. This collision time-scale is derived under an assumption that all the grains have a single grain radius a (A17). Since the grains have a large variety in grain radius, which radius we adopt to estimate above is not obvious. Thus, we simply estimate τ_{coll} around the medium grain radius, and adopt $\Delta t = \epsilon_\Delta \tau_{\text{coll}}$ with $\epsilon_\Delta = 0.3$. We denote the time-step determined in this way as $\Delta t_{\text{shat}} = (\epsilon_\Delta \tau_{\text{coll}})_{\text{shat}}^n$ and $\Delta t_{\text{coag}} = (\epsilon_\Delta \tau_{\text{coll}})_{\text{coag}}^n$ for shattering and coagulation, respectively. Because the collision time-scale is derived under an extreme assumption of single-sized grains, the time-step set in this manner usually gives satisfactorily short time-scale.

When implementing the grain size evolution in a hydrodynamical simulation, we update the grain size distribution at each hydrodynamical time-step Δt_{hydro}. For each process, if Δt_p (p is the process name 'acc', 'sput', 'shat', or 'coag') is shorter than Δt_{hydro}, we run sub-cycles for the grain size distribution with a time-step $\Delta t_{\text{hydro}}/n_{\text{sub}}$ that satisfies $\Delta t_p > \Delta t_{\text{hydro}}/n_{\text{sub}}$ (n_{sub} is the number of subcycles).

[8]There was a typo in Hirashita & Yan (2009).

APPENDIX C: EMPIRICAL FORMULA FOR THE GRAIN VELOCITY

We derive the empirical formula for the grain velocity (equation 18). We basically follow Ormel et al. (2009). The grain velocity is determined by grain–gas coupling through gas drag. The gas drag time-scale, τ_{dr}, is estimated as

$$\tau_{dr} = \frac{sa}{c_g \rho_g}, \tag{C1}$$

where c_g is the sound speed and ρ_g is the gas density. We assume that the turbulent velocity dispersion on a length scale of ℓ is described by the Kolmogorov spectrum:

$$v = v_{max} \left(\frac{\ell}{L_{max}} \right)^{1/3}, \tag{C2}$$

where v_{max} is the velocity at the size of the largest eddies, L_{max}. With this scaling relation, the turnover time, τ_{turn}, is estimated as

$$\tau_{turn} \equiv \frac{\ell}{v} = \frac{L_{max} v^2}{v_{max}^3}. \tag{C3}$$

A grain with a radius of a is coupled with the turbulence on the scale ℓ such that $\tau_{dr} = \tau_{turn}$. This leads to the following estimate using equations (C1) and (C3):

$$v = v_{max}^{3/2} \left(\frac{sa}{c_g \rho_g L_{max}} \right)^{1/2}$$

$$= \left(\frac{v_{max}}{c_g} \right)^{3/2} \left(\frac{L_{max}}{L_J} \right)^{-1/2} v_{gr,Ormel}, \tag{C4}$$

where $L_J \equiv (\pi c_g^2 / G \rho_g)^{1/2}/2$ is the Jeans length and $v_{gr,\,Ormel} \equiv c_g (sa/\rho_g L_J)^{1/2}$ is the grain velocity derived by Ormel et al. (2009), who assumed that $L_{max} = L_J$ and $v_{max} = c_g$ to obtain the grain velocity. We also adopt $L_{max} = L_J$ but relax the condition $v_{max} = c_g$ (we could move both quantities, but we move only v_{max} because they are degenerate). Using $\mathcal{M} \equiv v_{max}/c_g$, we obtain equation (18).

This paper has been typeset from a TEX/LATEX file prepared by the author.